Pericyte loss contributes to impaired venous drainage in a mouse model with Alzheimer's disease-like pathology

Andy Shih

Andy.Shih@seattlechildrens.org

Seattle Children's Research Institute https://orcid.org/0000-0002-7839-392X

Cara Nielson

Seattle Children's Research Institute https://orcid.org/0000-0002-6238-7824

Stephanie Bonney

https://orcid.org/0000-0002-9519-9272

Oron Estes

Seattle Children's Research Institute

Maria Sosa

Seattle Children's Research Institute

Article

Keywords: pericytes, Alzheimer's disease, capillary, cerebral blood flow

Posted Date: November 14th, 2025

DOI: https://doi.org/10.21203/rs.3.rs-8079147/v1

Additional Declarations: There is **NO** Competing Interest.

Pericyte loss contributes to impaired venous drainage in a mouse model with Alzheimer's disease-like pathology

Cara D. Nielson[1,2], Stephanie K. Bonney[1], Oron O. Estes[1], Maria J. Sosa[1], and Andy Y. Shih[1,3,4*]

[1] Center for Developmental Biology and Regenerative Medicine, Seattle Children's Research Institute, Seattle, WA, USA

[2] Graduate Program in Neuroscience, University of Washington, Seattle, WA, USA

[3] Department of Pediatrics, University of Washington, Seattle, WA, USA.

[4] Department of Bioengineering, University of Washington, Seattle, WA, USA.

Abstract: 180 words

Narrative: ~3400 words (Introduction, Results, Discussion)

References: 60

Figures: 7 main (all color); 11 supplementary (all color)

Keywords: pericytes, Alzheimer's disease, capillary, cerebral blood flow

Correspondence: Andy Y. Shih

Center for Developmental Biology and Regenerative Medicine

Seattle Children's Research Institute

1900 9th Ave. M/S JMB-5

Seattle, WA 98101

Office: 206-884-1314

Fax: 206-884-1407

Email: Andy.Shih@SeattleChildrens.org

ABSTRACT

The loss of brain pericytes occurs during aging and has been linked to vessel regression through changes in capillary flow patterns. However, the consequence of pericyte loss remains poorly understood in conditions involving amyloid-β burden. We performed *in vivo* two-photon imaging in the Tg-SwDI mouse model of Type-1 cerebral amyloid angiopathy and other aspects of Alzheimer's disease-like pathology to examine basal pericyte coverage and the effect of optically-induced pericyte loss. We find that spontaneous pericyte loss occurs preferentially on peri-venous capillaries in the somatosensory cortex of Tg-SwDI mice. Optically-induced pericyte ablation revealed slower structural remodeling of neighboring pericytes in Tg-SwDI mice, with the largest deficits seen in the peri-venous zone. Spontaneous pericyte loss in Tg-SwDI mice was associated with longer and more tortuous peri-venous capillaries indicative of vessel rarefaction. Mimicking peri-venous capillary regression by targeted optical ablation in wild-type mice reduced downstream blood flow by ~50-75%, while creating abnormal capillary flow heterogeneity upstream. These results suggest a selective vulnerability of the peri-venous zone in Type-1 cerebral amyloid angiopathy, and link pericyte loss to capillary rarefaction that may impair cerebral perfusion.

INTRODUCTION

The maintenance of adequate blood flow is critical for brain health, and cerebral hypoperfusion caused by various forms of cerebral small vessel disease contributes to accelerated cognitive decline. In fact, recent studies have demonstrated that vascular dysregulation is one of the earliest changes during the development of neurodegenerative disease.[1,2] The loss or dysfunction of brain pericytes is thought to play a key role in this vascular deficit.[3] Pericytes are mural cells embedded in the basement membrane of capillaries and transition zones between arterioles and venules.[4] They serve important roles in the maintenance of capillary tone and blood flow,[5–8] blood-brain barrier integrity,[9–11] and vascular network development.[12–14] Mice with a developmental loss of pericytes (null or hypomorphic alleles of PDGFRβ or reduced retention of endothelial-derived PDGFB) exhibit aberrant blood flow, hypoperfusion, and blood-brain barrier breakdown.[9,10,15,16] Newer mouse models using selective diphtheria-mediated ablation of pericytes in adulthood also exhibit blood-brain barrier breakdown and cerebral blood flow deficits, as well as leukocyte stalling, gliosis, and hypoxia[17–20] suggesting that pericyte coverage is important to maintain in the adult brain. Accordingly, reports of a ~20–60% reduction in brain pericyte density and coverage in post-mortem studies of the human Alzheimer's disease (AD) brain suggest substantial consequences on capillary architecture and perfusion *in vivo*.[21–23] However, this is difficult to study

in the living human brain, and the effects of pericyte loss during clinical AD have remained elusive. We therefore leverage live imaging in a mouse model of AD-like pathology to provide additional insight.

In prior studies, we induced pericyte loss in adult and aged mice using single-cell laser ablation. Consistent with their role in maintenance of basal capillary tone, pericyte loss led to the abnormal dilation of uncovered capillary regions, coupled with increased blood flow in dilated vessels.[5,6] An unexpected consequence of focal pericyte loss was diversion of blood from regions surrounding the dilated capillaries, resulting in a maldistribution of blood flow within the capillary network. Capillaries with reduced flow often stalled, leading to capillary regression and lasting reduction in vascular density and perfusion.[7] Critically, these studies also revealed that pericyte processes could remodel over days to restore endothelial coverage after pericyte loss. Neighboring pericytes extended their processes onto the uncovered endothelium, re-establishing basal lumen diameter and helping to normalize blood flow patterns.[5] Pericyte structural remodeling was diminished in the brains of aged mice, with the most severe deficits seen near the arteriole-capillary transition (ACT) zone.[7] However, AD pathology poses unique challenges to microvascular health, and our understanding of pericyte loss and structural remodeling in AD remains limited.

Tg-SwDI mice are a widely used model in preclinical AD research. These mice express the Swedish (K670N/M671L), and vasculotropic Dutch (E693Q) and Iowa (D694N) mutations of human amyloid precursor protein driven under the Thy1.2-promoter. Throughout the cortex, hippocampus, and thalamus, Tg-SwDI mice develop diffuse parenchymal amyloid-β (Aβ) plaques beginning around 3 months of age. By approximately 6 months of age, the mice develop fibrillar Aβ deposits on capillaries, known as Type-1 cerebral amyloid angiopathy (CAA), with greatest enrichment in thalamus and subiculum.[24–26] This capillary CAA extends into the cortex by 12 months of age and continues to advance with aging.[25] In the somatosensory cortex, 18-month-old Tg-SwDI mice exhibit pericyte loss and the shortening of pericyte processes.[27] In this study, we used *in vivo* two-photon microscopy to investigate how disease progression in the Tg-SwDI mouse model affects pericyte coverage, capillary network architecture, and perfusion in the cerebral cortex.

RESULTS

Loss of pericyte coverage occurs near ascending venules in Tg-SwDI mice.

We performed *in vivo* two-photon imaging on heterozygous Tg-SwDI mice crossed with tdTomato mural cell reporter mice to label pericytes (Tg-SwDI;PdgfrβCre-tdTomato mice).

Chronic cranial windows were implanted over the somatosensory cortex of 12–18-month-old Tg-SwDI;PdgfrβCre-tdTomato mice and wild-type (WT) age-matched controls **(Fig. 1a)**. The cortical vasculature was visualized with an i.v. injection of 70kDa FITC-dextran **(Fig. 1b).** Spontaneous pericyte loss was highly variable both within a single cranial window **(Supplemental Fig. 1a,b)** and between windows of individual mice **(Supplemental Fig. 1c,d)**, suggesting it is regionally heterogeneous and can be challenging to locate with *in vivo* imaging. However, 2 out of 6 Tg-SwDI mice imaged had large regions of uncovered vasculature within their cranial windows **(Fig. 1b,c)**. These uncovered vessels were preferentially found on branch orders 1-3 from ascending venules (AV), while little to no loss was observed on branch orders 1-3 from penetrating arterioles (PA) **(Fig. 1b,d)**. The sex of the animals was not related to basal pericyte loss. Further, no leakage of 70 kDa FITC-dextran was observed in covered or uncovered vessels, indicating a lack of overt blood-brain barrier breakdown **(Fig. 1a).** These data demonstrate that cortical pericyte loss occurs in the Tg-SwDI mouse model, consistent with prior histological studies,[27] but extend these findings by revealing heterogeneous pericyte loss concentrated around venules.

Pericyte remodeling is decreased in Tg-SwDI mice compared to age-matched controls.

In a subset of Tg-SwDI mice, we re-imaged regions of pericyte loss 12 weeks after initial imaging and found that they remained uncovered **(Fig. 1e),** suggesting that pericyte remodeling was compromised. To investigate pericyte remodeling capacity in Tg-SwDI animals, we induced targeted ablation of individual pericytes with two-photon irradiation, as previously described,[28] and measured the remodeling processes of neighboring pericytes over the span of 1 week (**Fig. 2a,b)**. Pericytes throughout the microvasculature beyond three branch orders from penetrating arterioles were targeted for ablation. The rate of pericyte process extension was significantly reduced in Tg-SwDI mice compared to age-matched controls **(Fig. 2c-f).** Similarly, the rate of vessel re-coverage by the synergistic growth of pericyte processes after ablation was significantly decreased **(Fig. 2g,h).** Out of 5 Tg-SwDI mice, the 2 mice with large regions of pericyte loss were among the 3 animals with the slowest average process extension rate. However, there was no correlation between the number of uncovered vessel segments at baseline and the average extension rate of pericyte processes in a mouse **(Fig. 2i.)**. The average extension rate of pericyte processes in each mouse was significantly slower in Tg-SwDI mice than WT controls, indicating that impaired pericyte remodeling was a feature of Tg-SwDI mice, irrespective of severity in basal loss of pericyte coverage **(Fig. 2j).** Of note, we occasionally observed the retraction of pericyte processes at 2 days post-ablation in Tg-SwDI mice (negative values), which were never observed in WT animals **(Fig. 2e,f, Supplemental Fig. 2a,b)**. Importantly, the irradiation parameters and the

characteristics of targeted pericytes were not different between groups **(Supplemental Fig. 3a-f).** These results demonstrate that following pericyte loss, Tg-SwDI mice do not re-establish pericyte coverage as efficiently as WT animals.

Capillary-venous transition zone pericytes in Tg-SwDI mice exhibit the largest growth deficits.

Given that basal loss of pericyte coverage tended to occur surrounding ascending venules, we examined whether optically-induced pericyte remodeling also varied with microvascular zone. We categorized our remodeling data based on the location of the remodeling pericyte somata. Pericytes in the arteriole-capillary transition (ACT) zone were within 3 branch orders from a PA, pericytes in the capillary-venous transition (CVT) zone were within 2 branch orders from an AV, and pericytes in the capillary zone were >3 branches from a PA and >2 branches from an AV **(Fig. 3a)**. Average growth rate of pericytes in the CVT zone was significantly slower in Tg-SwDI mice compared to age-matched controls, while the average growth rate of pericytes in the ACT and capillary zones was reduced, but did not reach significance between groups **(Fig. 3b-e, Supplemental Fig. 4a).** In Tg-SwDI mice, ~14% of ACT zone processes, ~32% of capillary zone processes, and ~45% of CVT zone processes had not finished growing by 7 days post-ablation, compared to ~16%, ~20%, and ~11%, respectively, of processes in WT mice **(Supplemental Fig. 4b).** These results further point to a selective vulnerability of pericytes in the CVT zone of Tg-SwDI mice.

Effects of pericyte loss on capillary diameter.

We previously showed that abnormal capillary dilation occurs after pericyte ablation and is effectively restored by pericyte remodeling in healthy adult mice.[5,6] However, pericyte remodeling does not restore capillary tone to basal levels in aged animals.[7] Thus, we examined capillary diameter changes following pericyte ablation in WT and Tg-SwDI mice **(Fig. 4a-e)**. At baseline, capillary diameter was similar between groups, 3.728 ± 0.8285μm (mean ± SD) in WT mice, and 3.941 ± 0.8730μm (mean ± SD) in Tg-SwDI mice, suggesting no disease-related capillary constriction at least in upper cortical layers. Consistent with prior studies in WT mice, capillaries dilated by ~36% following pericyte ablation and returned, on average, to baseline diameter following pericyte remodeling **(Fig. 4a,b,e,f,g).** In Tg-SwDI mice, vessels dilated by ~26% following pericyte ablation and remained dilated by ~9% following pericyte remodeling **(Fig. 4c,d,e,f,g).** However, these trends toward decreased dilation after pericyte loss and partial recovery after remodeling were not statistically significant. Lastly, vessels in Tg-SwDI mice

remained dilated if pericyte coverage was not re-established within 7 days **(Fig. 4h).**

Given the effects of focal pericyte ablation on vessel diameter, we sought to investigate how spontaneous pericyte loss in Tg-SwDI mice might alter capillary diameter. We measured vessel diameter in the CVT zone of WT and Tg-SwDI mice, as this region exhibited the largest number of uncovered vessels. Overall, there were no significant differences in the diameter of vessels between genotypes, and no significant differences between the covered and uncovered vessels in Tg-SwDI animals **(Fig. 4i-k).** Due to the high variability of diameter between individual vessels that could mask subtle changes, we examined the diameter of vessels with partial pericyte coverage and also found no significant changes in vessel diameter between pericyte covered and uncovered regions within the same vessel segment **(Fig. 4l,m).** Overall, these data reveal that spontaneous pericyte loss in Tg-SwDI mice do not elicit overt capillary dilations.

Pericyte loss is associated with longer and more tortuous capillaries.

We previously showed that pericyte loss alters the architecture of the microvascular network. When uncovered capillaries dilate, they divert blood from surrounding vessels, creating a flow imbalance where low-flow vessels may stall and regress.[7] To examine structural changes in capillaries following spontaneous pericyte loss, we measured the length and tortuosity of the vessels in the CVT zone **(Fig. 5a, b)**. We found no overall differences between the length of WT and Tg-SwDI vessels, while there was a trend towards Tg-SwDI vessels being more tortuous than WT vessels **(Fig. 5c).** However, vessels with partial pericyte coverage in Tg-SwDI mice (>10um of vessel with coverage) were significantly longer and more tortuous than fully uncovered vessels and covered vessels **(Fig. 5a, b, d, Supplemental Fig. 6a, b)**. This indicated that pericyte loss may be leading to the regression of uncovered vessels. Indeed, in a subset of Tg-SwDI mice imaged longitudinally ~3 months apart, we observed regression of 4 uncovered peri-venous capillaries **(Fig. 5e)** and no regression of pericyte-covered vessels**.** Thus, we propose a hypothetical model where pericyte loss in peri-venous capillaries leads to vessel regression, resulting in remaining vessels with partial pericyte coverage and a longer and more tortuous route for blood flow **(Fig. 5f)**.

Given that capillary stalling can lead to vessel regression,[7,29,30] we examined the number of vessel stalls in WT and Tg-SwDI mice. However, there were similar levels of capillary stalls between genotypes that occurred preferentially in the capillary and CVT zones **(Supplemental Fig. 7a-e)**. These results suggest that pericyte loss likely precedes vessel regression in Tg-SwDI mice and may be independent of capillary stalling. It is also possible that our imaging strategy was not optimized to capture stalling events, as individual capillaries could only be assessed over

short time periods within z-stacks.

Capillary regression leads to blood flow reduction in downstream vessels.

Redundancy of blood flow routes in capillary networks offer resilience to loss of individual vessel segments.[31] However, CVT zones are bottlenecks for blood efflux from cortex. To test whether peri-venous capillary regression could contribute to impaired blood flow, we induced capillary regression in healthy adult mural cell reporter mice (PdgfrβCre-tdTomato) through capillary injury, as previously described.[32] Capillaries located 2 branch orders from an ascending venule, sites of observed regression in Tg-SwDI mice, were selectively ruptured using a precision high power laser line scan. Sham injuries were performed by targeting the laser onto parenchymal regions adjacent to vessel segments **(Fig. 6a, b)**. There were no significant differences in irradiation power, irradiation time, and cortical depth or diameter of target vessels between injuries or sham experiments **(Supplemental Fig. 8a-d)**. Red blood cell (RBC) flux and capillary diameter were then measured in the vessels upstream and downstream of the target vessel at baseline, 5 minutes post-injury, and 3- and 21-days post-injury.

On average, RBC flux declined significantly by ~50-75% from baseline levels at 5 min and 21 days post-injury in the vessel segment downstream of the injury, which drains directly into the ascending venule **(Fig. 6c, d, Supplemental Fig. 9a)**. In contrast, no significant flow changes were observed in sham-irradiated mice**.** In some cases, flow in downstream vessels stopped completely, indicating that the ablated vessel segment was the dominant blood supply, and re-routing of flow around the ablated vessel segment was inefficient. These reductions in RBC flux were not accompanied by significant changes in downstream vessel diameter, indicating that flux changes were a consequence of limited vascular interconnectivity, as opposed to vasoconstrictive responses to injury **(Fig. 6e, f, Supplemental Fig. 9b).** Prior to manipulation, the downstream vessels were not different in RBC flux between regression and sham experiments **(Supplemental Fig. 9a).** Overall, these data suggest that peri-venous capillaries are bottlenecks for blood efflux from cortex and loss of a branch within the CVT zone is sufficient to cause flow resistance**.**

To understand the broader effects of peri-venous capillary ablation on blood flow, we also examined flow changes in vessels directly upstream of the regression **(Fig. 7a).** Compared to sham irradiated vessels, upstream vessels normally flowing into the irradiated vessel segment tended to decrease in flux, while those flowing away exhibited more variable changes **(Fig. 7b, Supplemental Fig. 10a, c, Supplemental Fig. 11a, b)**. As a result, the heterogeneity of flux among upstream capillaries increased significantly in regression experiments, despite modest, non-significant changes to vessel diameter (**Fig 7b, c, Supplemental Fig. 10b, d, Supplemental**

Fig. 11a, b).

Increased capillary flow heterogeneity may contribute to poorer oxygen distribution and impaired oxygen extraction during functional hyperemia.[33–38] To better understand this heterogeneity, we considered the diameter of upstream vessels. When flow from a larger diameter capillary was forced to flow into a smaller diameter capillary, then flow would decrease due to higher resistance. Conversely, if flow from a smaller diameter capillary was forced to flow into a larger diameter capillary, then blood flow would increase due to a lower resistance **(Fig. 7d, e)**. As a result, there was a trend toward positive correlation between change in RBC flux and diameter difference between the upstream vessels at 21 days post-injury (**Fig. 7e**). All examined vessels flowing into smaller diameter capillaries decreased in RBC flux, while vessels flowing into larger diameter capillaries increased in RBC flux 62.5% of the time **(Fig. 7f).** These results demonstrate how vessel regression near venules can lead to local flow heterogeneity in capillary networks, likely creating regions of poorer tissue oxygenation.

DISCUSSION

Our results highlight a potential mechanism by which pericyte loss could contribute to cerebral hypoperfusion in AD. Our *in vivo* imaging studies in Tg-SwDI mice revealed a unique susceptibility of pericytes in the CVT zone. When pericyte loss was observed, it was concentrated around cortical ascending venules. Pericytes near venules also showed impaired capacity to remodel, leading to prolonged loss of endothelial coverage. Changes in capillary structure were consistent with regression of peri-venous capillaries following pericyte loss, and this was directly observed in a subset of cases. Mimicking capillary regression in the CVT zone of healthy mice caused a ~50–75% reduction in downstream blood flow and greater flow heterogeneity in the upstream capillary network. These findings suggest that pericyte loss may be a contributing factor to the capillary rarefaction seen in models of AD-like pathology[39–42], and dysfunction near venules have an outsized effect on local blood flow since they are bottlenecks for blood efflux.

While the cause of pericyte vulnerability in the CVT zone remains unclear, there are several possibilities. Post-capillary venules are the preferential site of leukocyte trafficking across the endothelium, mediated by an upregulation of adhesion molecules ICAM and VCAM in endothelial cells.[43,44] The upregulation of leukocyte adhesion molecules has been shown in aging, AD, and mouse models of pericyte loss.[10,19,45–48] Heightened leukocyte recruitment is linked to the secretion of reactive oxygen species and toxic pro-inflammatory cytokines, such as IL-8, TNF-α, and IL-1β,[49,50] which exacerbate neuroinflammation and could cause pericyte dysfunction and cell

death. Another possible contributor to CVT zone dysfunction is the disruption of glymphatic clearance, or accumulation of waste solutes exiting out of the brain via para-venous pathways,[51] which has been shown to be impaired in the APP/PS1 mouse model of AD.[52] It is also possible that pericyte loss in the CVT zone is secondary to other causes of hypoperfusion, but subsequently exacerbates hypoperfusion by impairing blood drainage.[53–55] In general, tissues and vasculature surrounding venules experience lower oxygen levels because they are farthest from the arteriolar oxygen source.

Capillaries lacking pericyte coverage under basal conditions were not overtly dilated in Tg-SwDI mice. However, optical pericyte ablation elicited consistent capillary dilations. The basis for this discrepancy is not clear, but it is possible that endothelial dysfunction in AD[47,56,57] causes stiffening of the capillary wall, making dilation less evident. Consistent with this idea, optical ablation of pericytes in Tg-SwDI mice dilated capillaries ~10% less than in WT controls, on average, with some vessels even constricting from baseline. Compensatory mechanisms may also be involved over the longer term, such as re-structuring of the endothelial cytoskeleton to maintain capillary tone in the absence of pericytes. Future longitudinal *in vivo* imaging studies are needed to observe vascular changes throughout disease progression.

Vessel regression following capillary injury increased blood flow heterogeneity among upstream capillaries and reduced efflux into the downstream venule. The remaining capillaries also become longer and more tortuous due to loss of branchpoints. These alterations are expected to increase the capillary transit time heterogeneity for RBCs by forcing more circuitous flow paths. Elevated capillary transit-time heterogeneity reduces oxygen extraction and prevents the optimal homogenization of capillary flux that normally enhances oxygen extraction during functional hyperemia.[33–37] Moreover, capillary pericytes in the CVT zone can regulate capillary tone through contractile signaling and may enable subtle diameter adjustments that support flux homogenization.[38] Thus, the loss of pericyte coverage in AD could impair this dynamic regulation. Overall, increased capillary transit-time heterogeneity has been documented in AD patients compared to healthy controls[55] and our results implicate pericyte loss and vessel rarefaction as contributors to these capillary flow disturbances in AD.

There are some limitations to our study. The variability in pathology between cranial windows of individual Tg-SwDI mice made it difficult to fully understand the etiology of the disease. In addition, vessel diameters for genotype comparison were measured in anesthetized mice, and it is possible that the vasodilatory effects of isoflurane differentially affect vessels with and without pericyte

contact. Finally, while we did not observe an increase in capillary stalling between WT and Tg-SwDI mice, our observations were made in z-stacks with limited sampling time on each vessel, which reduces the change of detecting flow stalls.

Venules and the CVT zone remain underexplored components of cerebral microvasculature. Although human neuropathology studies of AD frequently report pericyte loss,[21–23] this pathology has not been examined in relation to defined vascular zones. Murine studies are providing some deeper insight. In a separate mouse model of AD, mural cell loss along venules was observed, and venous structure abnormalities markedly worsen with blockade of PDGFRβ signaling, a pathway central to mural cell function.[58] We also recently demonstrated that capillaries draining into principal cortical venules of layer 6 and corpus callosum preferentially lose pericyte coverage with normal aging in mice.[59] However, these prior observations were limited by their cross-sectional nature. Future longitudinal imaging studies will be critical for defining the etiology and consequence of pericyte dysfunction within the CVT zone of Tg-SwDI mice, as well as in complementary AD models. In parallel, tissue clearing and light-sheet microscopy will provide essential 3D data to localize pericyte loss across microvascular beds beyond the cerebral cortex in mice, and ultimately in human AD specimens. Finally, determining the molecular mechanisms that regulate pericyte structural remodeling remains imperative, as promoting enhancing pericyte coverage and may improve capillary network perfusion and oxygen delivery to the brain.

MATERIALS & METHODS

Animals. Mice were housed in specific-pathogen-free facilities approved by AALAC and were handled in accordance with protocols approved by the Seattle Children's Research Institute IACUC committee. PdgfrβCre-tdTomato mice were created by breeding Pdgfrβ-Cre mice (FVB and C57BL/6 × 129 background) with Ai14-flox (Jax #007914) mice (C57BL/6 background) to generate a mural cell reporter line. PdgfrβCre-tdTomato mice were crossed with Tg-SwDI (Jax #034843) mice (C57BL/6 background) to label mural cells in a mouse model of Aβ pathology. Age-matched animals negative for the Tg-SwDI gene were used as experimental controls. Pdgfrβ-Cre mice were a generous gift from Prof. Volkhard Lindner of the Maine Medical Center Research Institute. Both male and female mice were utilized. For pericyte ablation experiments: n=3 female mice and 2 male mice per group. For analysis of pericyte coverage, length, and tortuosity: Wild-type n=3 female mice and 4 male mice, Tg-SwDI n=3 female mice and 3 male mice. For analysis of vessel diameter and stalling: Wild-type n=3 female mice and 3 male mice, Tg-SwDI n=3 female mice and 3 male mice. Only female PdgfrβCre-tdTomato mice (n=3) were utilized in capillary

injury experiments due to availability of animals. At the time of imaging, Tg-SwDI;PdgfrβCre-tdTomato mice were between 12-18 months and PdgfrβCre-tdTomato mice were between 4-8 months.

Cranial window surgery and in vivo two-photon imaging. Chronic, skull-removed cranial windows were placed over the somatosensory cortex for in vivo imaging, as previously described.[5] Mice were allowed to recover for at least three weeks prior to imaging. For vascular labeling, mice were injected with 50μL of 5% (w/v in saline) 70kDa FITC-dextran (Sigma-Aldrich; 46945) through the retro-orbital vein under deep isoflurane anesthesia (4% MAC in medical-grade air). During imaging, isoflurane was maintained at ~1.5-2% MAC in medical-grade air. Imaging was performed with a Bruker Investigator coupled to a Spectra-Physics Insight X3. Collection of green and red fluorescence emission was achieved with 525/70 and 595/50 emission bandpass filters respectively and detected with GaAsP photomultiplier tubes. A 20x (1.0 NA) water-immersion objective (Olympus; XLUMPLFLN) was used to collect high-resolution images. Z-stacks were collected at 1.0μm increments at 3.6 μs/pixel dwell time and 975 nm excitation.

Pericyte ablation with two-photon irradiation. Pericytes to target for ablation were chosen by identifying cells >3 branch orders from a penetrating arteriole, <150μm from the cortical surface, and exhibiting a bump-on-a-log morphology (targetable without hitting the underlying vessel). Injuries were induced by delivering ~50-100mW of power at 725nm excitation directly onto the pericyte soma using the line-scan function for a total of ~60-100s, in 20s increments, at 3.6μs/pixel dwell time.[28] Z-stacks were collected prior to ablation, 5 minutes post-ablation, and then either 2, 4, and 7 days post-ablation, or 3 and 7 days post-ablation.

Analysis of pericyte remodeling and vessel coverage. To analyze pericyte remodeling following pericyte ablation, remodeling processes were first identified by determining which surviving processes had lost pericyte contact at their terminal tips. Then, using the simple neurite tracer (SNT) plugin in FIJI, process length was measured from soma to process terminus at each imaging time point in 3D.[5,28] Process extension was calculated by subtracting process length at baseline from process length at each imaging time point. Vascular length uncovered by pericytes at each time point was also measured using SNT. Vessel re-coverage was calculated by subtracting the uncovered vessel length at each timepoint from the baseline uncovered length which was discernable 5 minutes post-ablation. Pericytes within 3 branch orders of a penetrating arteriole were classified as ACT zone cells, pericytes within 2 branch orders of an ascending venule were classified as CVT zone cells, and pericytes >3 branch orders from a penetrating

arteriole and >2 branch orders from an ascending venule were classified as capillary zone cells. Processes were excluded from zonation analysis if their location could not be determined, for example, if they were near the edge of an imaging frame or bottom of a z-stack.

Analysis of vessel diameter. The VasoMetrics FIJI plugin[60] was utilized to measure vessel diameter on max projections of each vessel segment. For diameter measurements in awake mice (**Fig.6-7, Supplemental Fig.8-11**), any imaging frames where the animal had moved were excluded from the z-stacks to ensure accurate measurements.

Quantification of vessel length and tortuosity. The SNT plugin in FIJI was used to trace vessel segments from one branch point to the next and measure both the vessel length and tortuosity of each segment. The "path length" and "branch contraction" SNT outputs were recorded, and tortuosity was calculated by taking the inverse of the branch contraction (the Euclidean distance of a branch divided by its path length).

Quantification of capillary stalling. Z-stacks were carefully examined image by image and vessels without blood flow were identified. Vessel segments were considered stalled if they were either plugged (had a dark shadow occupying part of the vessel segment) or had only blood plasma present and no red blood cells could be seen moving through the vessel. The number of stalls was normalized to the volume of each z-stack.

Capillary injuries with two-photon irradiation. PdgfrβCre-tdTomato mice were briefly anesthetized with 4% MAC in medical-grade air and head-fixed to a treadmill (PhenoSys speedbelt) allowing forward and backward movement. Following i.v. dye injection, animals were removed from isoflurane and allowed to wake up from anesthesia for at least 10 minutes prior to the start of imaging. Capillary segments to target for injuries were chosen by identifying capillary segments both within the upper 100μm of cortex and 2 branch orders from an ascending venule. Injuries were induced by creating a circular line-scan path slightly larger than the diameter of the capillary and applying ~100-200mW of power at 800nm excitation directly onto the vessel for ~60-160s in 20s increments at 3.6μs/pixel dwell time.[32] Scanning was ceased when leakage of i.v. dye was detected and the vessel was no longer flowing. Sham injuries were performed in separate vascular networks by focusing the laser on a parenchymal region adjacent to a capillary segment using similar parameters as described above. Z-stacks were collected prior to injury, and 5 min, 3 days, and 21 days post-injury.

Blood flow analysis. In awake PdgfrβCre-tdTomato mice, line-scans were collected in the capillary

segments surrounding the injured or sham irradiated vessel segment. 1.3 s line-scans of each segment were collected prior to injury, and 5 min, 3 days, and 21 days post-injury. 3 line-scans were taken per segment. RBC flux was measured by counting the number of RBC shadows in each line-scan using the CellCounter plugin in FIJI and normalizing the numbers to line-scan time. Measurements from the 3 line-scans per segment were averaged to achieve the final RBC flux.

Statistics. All statistical analyses were performed in Graphpad Prism (v.10.2.1) or SPSS (v.31). Respective statistical analyses are reported in each figure legend. Shapiro-Wilk tests of normality were performed on necessary data sets prior to statistical analysis. Unless specified otherwise, normally distributed data with multiple measurements per animal were analyzed with nested tests in GraphPad Prism. Non-normally distributed data and data to be analyzed with a two-way design with multiple measurements per animal were assessed for between mouse variability with a chi-square test in GraphPad Prism and data without significant variability between mice was pooled for analysis and analyzed with the appropriate test in GraphPad Prism, while data with significant variability between mice was analyzed with a mixed-effects model in SPSS with mouse as a random factor. Standard deviation is reported in all graphs where necessary.

ACKNOWLEDGMENTS

We would like to thank Hyun-Kyoung Lim, Stefan Stamenkovic, and Jule Gust for feedback on the manuscript and Liam Sullivan and Taylor McGillis for technical support. CDN was supported by a NIH training grant (T32AG052354). SKB was supported by fellowships from the NIH/NINDS (F32NS117649) and NIH/NIA (K99AG080034). MJS was supported by a Diversity supplement for a grant from the NIH/NIA (R01AG062738-05S1). AYS and projects in the Shih lab were supported by grants from the NIH/NIA (R01AG062738, R21AG069375, RF1AG077731, R01AG081840) and the Leducq foundation (23CVD03).

AUTHOR CONTRIBUTIONS

CDN, SKB, and AYS conceptualized and designed experiments. Experiments and data analysis were performed by CDN, OOE, SKB and MJS. Manuscript was written by CDN and AYS with editing and contributions from all authors.

DATA AVAILABILITY

Source data is included with this manuscript. Due to their large size, images are stored on a server at Seattle Children's Research Institute and will be provided upon request.

COMPETING INTERESTS

The authors have no financial or non-financial competing interests to disclose.

FIGURE LEGENDS

Figure 1. Uncovered capillaries in Tg-SwDI mice are found closer to the venule side of the microvascular network. a) Schematic of in vivo two-photon imaging and breeding scheme for experiments. **b)** Representative *in vivo* two-photon image of cortex from a wild-type (WT) mouse and a Tg-SwDI mouse with pericyte loss in peri-venous capillaries. Vessels shown in green and mural cells shown in red. Regions lacking pericyte coverage indicated with white dotted lines. AV=ascending venule. PA=penetrating arteriole. Scale bar=50μm. **c)** Graph showing the total number of vessel segments lacking pericyte coverage in WT and Tg-SwDI mice. Two-tailed Mann-Whitney test: p=0.3619. WT n=7 mice, Tg-SwDI n=6 mice. Data shown as mean ± SD. **d)** Graph showing the number of vessel segments lacking pericyte coverage in WT and Tg-SwDI mice sorted by branch order from penetrating arteriole (A) or ascending venule (V). Two-way ANOVA with Sidak's multiple comparisons: Effect of genotype: $F(1,66)=5.823$, *p=0.0186, Effect of location: $F(5,66)=1.403$, p=0.2348, interaction: $F(5,66)=1.141$, p=0.3478. WT n=7 mice, Tg-SwDI n=6 mice. Data shown as mean ± SD. **e)** Representative images of uncovered vessels in a Tg-SwDI mouse 12 weeks apart. Vessels shown in green and mural cells shown in red. AV=ascending venule. Scale bar=20μm.

Figure 2. Pericyte remodeling rate is decreased in Tg-SwDI mice. a) Schematic of a pericyte ablation showing target pericyte (left), uncovered vasculature following ablation (right, purple), and remodeling pericytes (right, pink). Black arrows=direction of process growth. **b)** Example *in vivo* images of a pericyte (red) and vessel (green) before and 5 minutes post-ablation. Yellow line=ablative line-scan path. Scale bar=10μm. **c,d)** Representative examples of pericyte remodeling in a WT (c) and Tg-SwDI (d) mouse. In top panels, pericytes shown in red and vessels shown in green. In the bottom panels, only mural cells are shown. White asterisk=target pericyte. Schematics of pericyte remodeling over time depicted under images with vessels in green and pericyte processes in pink. Scale bar=50μm. **e)** Graphs of individual pericyte process extension over time in WT (left) and Tg-SwDI (right) mice. **f)** Graph of average pericyte process growth rate in each genotype. Two-tailed Mann-Whitney test: ***p=0.002. Data shown as mean ± SD. n=5 mice/group (86 processes from 23 WT ablations and 69 processes from 20 Tg-SwDI ablations). **g)** Graph of the average rate of vessel re-coverage in each genotype. Two-tailed, nested t-test:

F(1,41)=7.011, *p=0.0114. Data shown as mean ± SD. n=5 mice/group (23 WT ablations and 20 Tg-SwDI ablations). **h)** Graph of vascular re-coverage over time after pericyte ablation in WT (left) and Tg-SwDI (right) mice. **i)** Correlation plot of the number of vessel segments lacking pericyte coverage vs. the average growth rate of pericyte processes per mouse in each genotype. Two-tailed Pearson correlation tests. R and p values reported on graph. n=5 mice/group. **j)** Graph of average pericyte process growth rate per mouse in each genotype. Two-tailed, unpaired t-test: F(4,4)=4.698, *p=0.0167. n=5 mice/group.

Figure 3. The capillary-venous transition zone exhibits the largest pericyte remodeling deficit in Tg-SwDI mice. a) Schematic of each zone of the cortical microvascular network. The ACT zone was classified as branch orders 1-3 from a penetrating arteriole (PA), the CVT zone was classified as the ascending venule (AV) and branch orders 1-2 from an AV, and the capillary zone was classified as vessels >3 branch orders from a PA and >2 branch orders from an AV. In left panels, vessels shown in green and mural cells shown in red. Right panels show only mural cell channel. Scale bar=20μm. **b,c)** Representative examples of a remodeling pericyte in the CVT zone in a (b) WT and (c) Tg-SwDI mouse. In top panels, pericytes shown in red and vessels shown in green. Bottom panels show mural cell channel only. Arrowhead indicates the soma of the remodeling pericyte. Magenta bar indicates baseline process length to demonstrate growth of process over time. Pericyte-pericyte contact (pc-pc contact) is indicated with a blue arrowhead. AV=ascending venule. Scale bar=20μm. **d)** Graph of the average pericyte process growth rate of pericytes in each microvascular zone across WT and Tg-SwDI mice. Two-way ANOVA with Sidak's multiple comparisons: effect of genotype: F(1,139)=6.571, *p=0.0114, effect of zone: F(2,139)=0.9413, p=0.3926, interaction: F(2,139)=0.8459, p=0.4314. ACT zone WT vs. Tg-SwDI: p=0.7201, capillary zone WT vs. Tg-SwDI: p=0.2882, CVT zone WT vs. Tg-SwDI: **p=0.0083. n=5 mice/group (23 WT ablations and 20 Tg-SwDI ablations). Data shown as mean ± SD. **e)** Graph of individual pericyte process extension across the ACT zone (top), capillary zone (middle), and CVT zone (bottom).

Figure 4. Pericyte ablations and spontaneous pericyte loss elicit different effects on capillary diameter. a) Images of WT vessels throughout pericyte remodeling. In top panels, vessels shown in green and pericytes shown in red. In lower panels, vessels shown in grey. Scale bar=20μm. **b)** Graph of WT capillary diameter throughout pericyte remodeling. Linear mixed effects model with Sidak's multiple comparisons: Effect of coverage: F(2,46.645)=32.015, ***p=<0.001, pre vs. uncovered: ***p<0.001, uncovered vs. recovered: ***p<0.001, pre vs.

recovered: p=0.942. n=5 WT mice (23 capillaries). **c)** Images of Tg-SwDI vessels after pericyte ablation and remodeling. In top panels, vessels shown in green and pericytes shown in red. In bottom panels, vessels shown in grey. Scale bar=20μm. **d)** Graph of Tg-SwDI capillary diameter throughout pericyte remodeling. Friedman test with Dunn's multiple comparisons: Effect of coverage: ****p<0.0001, pre vs. uncovered: ****p<0.0001, uncovered vs. recovered: *p=0.0449, pre vs. recovered: p=0.1547. n=5 Tg-SwDI mice (19 capillaries). **e)** Insets from (a) and (b). Dashed magenta lines=baseline diameter. Scale bar=20μm. **f)** Graph of percent change in capillary diameter post-ablation. Two-tailed Nested t-test: F(1,8)=1.992, p=0.1958. n=5 mice/group (23 WT and 34 Tg-SwDI capillaries). **g)** Graph of percent change from baseline to re-covered diameter. Two-tailed Nested t-test: F(1,8)=2.321, p=0.1661. n=5 mice/group (49 WT and 25 Tg-SwDI capillaries). **h)** Graph of capillary diameter in Tg-SwDI mice at baseline, 2-3 days after losing pericyte coverage, and 7 days after losing pericyte coverage. Friedman test with Dunn's multiple comparisons: Effect of coverage: ****p<0.0001, pre vs. 2-3 days: ****p<0.0001, 2-3 days vs. 7 days: p>0.9999, pre vs. 7 days: ***p=0.0002. n=5 Tg-SwDI mice (21 capillaries). **i)** Images of capillaries in WT and Tg-SwDI mice. In top panels, vessels shown in green and pericytes shown in red. In lower panels, vessels shown in grey. White arrowheads=uncovered vessels. AV=ascending venule. Scale bar=20μm. **j)** Capillary diameter of CVT zone vessels in WT and Tg-SwDI mice. Gamma mixed model: F(1,2551)=0.001, p=0.980. n=6 mice/group (864 WT and 1689 Tg-SwDI capillaries). **k)** Graph of capillary diameter of covered and uncovered CVT zone vessels in Tg-SwDI mice. Gamma mixed model: F(1,1687)=1.074, p=0.300. n=6 Tg-SwDI mice (1491 covered and 198 uncovered capillaries). **l)** Images of partially covered vessels in Tg-SwDI mice. In top panels, vessels shown in green and pericytes shown in red. In bottom panels, vessels shown in grey. White lines indicate where corresponding diameter measurements were taken. AV=ascending venule. Scale bar=20μm. **m)** Graph of partially covered vessel diameter. Wilcoxon matched-pairs signed rank test: p=0.8904. n=4 Tg-SwDI mice (26 capillaries). All error bars indicate mean ± SD.

Figure 5. Spontaneous pericyte loss may lead to vessel regression. a) Images of fully uncovered vessels in Tg-SwDI mice. In the left panels, vessels shown in green and pericytes shown in red. In the right panels, vessels shown in grey. Examples of uncovered vessels traced in blue. AV=ascending venule. Scale bar=20μm. **b)** Images of partially uncovered vessels in Tg-SwDI mice. In the left panels, vessels shown in green and pericytes shown in red. In the right panels, vessels shown in grey. Examples of partially uncovered vessels traced in pink. AV=ascending venule. Scale bar=20μm. **c)** Graph of length (left) and tortuosity (right) of all CVT zone vessels in WT and Tg-SwDI mice. Gamma mixed model for length: $F(1,3323)=0.003$, $p=0.954$. Gamma mixed model for tortuosity: $F(1,3323)=1.749$, $p=0.186$. n=7 WT and 6 Tg-SwDI mice (1133 WT capillaries, 2192 Tg-SwDI capillaries). Data shown as mean ± SD. **d)** Graph of length (left) and tortuosity (right) of covered, uncovered, and partially covered CVT zone vessels in Tg-SwDI mice. Gamma mixed models with Sidak's pairwise comparisons: Effect of pericyte coverage on length: $F(2,2189)=27.426$, ***p=<0.001, covered vs. uncovered: **p=0.006, covered vs. partially covered: ***p<0.001, uncovered vs. partially covered: ***p<0.001. Effect of pericyte coverage on tortuosity: $F(2,2189)=19.731$, ***p=<0.001, covered vs. uncovered: p=0.421, covered vs. partially covered: ***p<0.001, uncovered vs. partially covered: ***p<0.001. n=6 Tg-SwDI mice (1975 covered, 165 uncovered, 52 partially uncovered). Data shown as mean ± SD. **e)** Four examples of uncovered vessels in Tg-SwDI mice regressing after 12 weeks. Vessels shown in green and pericytes shown in red. AV=ascending venule. Scale bar=20μm. **f)** Schematic of a hypothetical model of vessel regression following pericyte loss. Pericytes shown in red and vessels shown in black.

Figure 6. Capillary regression in CVT zone reduces blood flow into downstream drainage vessels. a) Schematic of optically-induced capillary injury in the CVT zone. **b)** Example of a capillary regression (top) and a sham (bottom) prior to, 5 min post, and 21 days post-injury. Blue circles = line-scan path, blue arrows = downstream vessel, white arrows = blood flow direction, AV=ascending venule. Vessels shown in grey. **c)** Graph of the percent change from baseline in downstream vessel RBC flux 5 min and 21 days post-injury. Two-way repeated measures ANOVA with Sidak's multiple comparisons: Effect of injury type: $F(1,13)=13.81$, **p=0.0026, effect of time: $F(1,13)=0.1296$, $p=0.7247$, interaction: $F(1,13)=11.01$, **p=0.0056. Sham vs. regression 5 min post-injury: ***p=0.0002, sham vs. regression 21 days post-injury: p=0.0709. **d)** Graphs of the percent change from baseline in downstream vessel RBC flux 5 min and 21 days post-injury in sham (left) and regression (right) experiments. Two-way repeated measures ANOVA with Sidak's multiple comparisons: Effect of injury type: $F(1,13)=13.81$, **p=0.0026, effect of time:

F(2,26)=4.024, *p=0.0300, interaction: F(2,26)=12.90, ***p=0.0001. Regression experiments: Pre vs. 5 min post-injury: ****p<0.0001, pre vs. 21 days post-injury: **p=0.0023. Sham experiments: Pre vs. 5 min post-injury: p=0.1320, pre vs. 21 days post-injury: p=0.9889. **e)** Graph of the percent change from baseline in downstream vessel diameter 5 min and 21 days post-injury. Linear mixed-effects model: Effect of injury type: F(1,13)=1.440, p=0.2515, effect of time: F(1,12)=0.1980, p=0.6643, interaction: F(1,12)=0.03028, p=0.8648. **f)** Graphs of the percent change from baseline in downstream vessel diameter 5 min and 21 days post-injury in sham (left) and regression (right) experiments. Linear mixed-effects model: Effect of injury type: F(1,13)=1.969, p=0.1839, effect of time: F(2,25)=1.551, p=0.2317, interaction: F(2,25)=0.7916, p=0.4642. All data shown as mean ± SD. n=3 mice, 4-6 injuries/mouse.

Figure 7. Capillary regression alters flow in upstream vessels. a) Representative example of a capillary network targeted for regression experiments. The blue arrowhead depicts the target vessel. The magenta arrowheads depict the upstream vessels. The direction of blood flow is shown with white arrows. AV = ascending venule. Vessels shown in grey. Scale bar=20μm. **b)** Graph of percent change in RBC flux in upstream vessels at 5 min and 21 days-post injury. Two-way repeated-measures ANOVA: Effect of injury type: F(1,26)=0.3793, p=0.5433, effect of time: F(1,26)=0.0007258, p=0.9787, interaction: F(1,26)=0.1251, p=0.7264. Welch's F-test: 5 min post: F(13,13)=4.704, **p=0.0088 and 21 days post: F(13,13)=3.265, *p=0.0416. Data shown as mean ± SD. N=3 female mice, 2-3 capillary injuries and shams per mouse. **c)** Graph of percent change in vessel diameter in upstream vessels at 5 min and 21 days-post injury. Linear mixed model: Effect of injury type: F(1,48.182)=0.226, p=0.637, effect of time: F(1,47.989)=0.684, p=0.412, interaction: F(1,47.989)=0.063, p=0.802. Welch's F-test: 5 min post: F(11,13)=6.314, **p=0.0026, and 21 days post: F(11,13)=3.662, *p=0.0295. Data shown as mean ± SD. N=3 female mice, 2-3 capillary injuries and shams per mouse. **d)** Schematic of blood flow changes after capillary regression. Blood flow in the vessel downstream of the target vessel is consistently reduced. Upstream, if blood is flowing into a smaller diameter vessel, resistance increases and RBC flux decreases. Conversely, if blood is flowing into a larger diameter vessel, resistance decreases and RBC flux increases. **e)** Graph of diameter difference of upstream vessels vs. percent change in RBC flux from baseline at 21 days post-injury. One-tailed Spearman correlation. R and p values reported on graph. n=14 pooled vessels from 7 regression experiments across 3 mice. **f)** Graph of the proportion of upstream vessels that decrease (blue) or increase (red) in flux compared between cases of flow into larger vessels versus flow into smaller vessels. One-sided Fisher's exact test: ****p<0.0001. n=14 pooled vessels from 7 regression experiments across 3 mice.

REFERENCES

1. Wierenga, C. E., Hays, C. C. & Zlatar, Z. Z. Cerebral blood flow measured by arterial spin labeling MRI as a preclinical marker of Alzheimer's disease. *J. Alzheimers Dis. JAD* **42 Suppl 4**, S411-419 (2014).
2. Iturria-Medina, Y. *et al.* Early role of vascular dysregulation on late-onset Alzheimer's disease based on multifactorial data-driven analysis. *Nat. Commun.* **7**, 11934 (2016).
3. Korte, N., Nortley, R. & Attwell, D. Cerebral blood flow decrease as an early pathological mechanism in Alzheimer's disease. *Acta Neuropathol. (Berl.)* **140**, 793–810 (2020).
4. Ornelas, S. *et al.* Three-dimensional ultrastructure of the brain pericyte-endothelial interface. *J. Cereb. Blood Flow Metab.* **41**, 2185–2200 (2021).
5. Berthiaume, A.-A. *et al.* Dynamic Remodeling of Pericytes In Vivo Maintains Capillary Coverage in the Adult Mouse Brain. *Cell Rep.* **22**, 8–16 (2018).
6. Hartmann, D. A. *et al.* Brain capillary pericytes exert a substantial but slow influence on blood flow. *Nat. Neurosci.* **24**, 633–645 (2021).
7. Berthiaume, A.-A. *et al.* Pericyte remodeling is deficient in the aged brain and contributes to impaired capillary flow and structure. *Nat. Commun.* **13**, 5912 (2022).
8. Hall, C. N. *et al.* Capillary pericytes regulate cerebral blood flow in health and disease. *Nature* **508**, 55–60 (2014).
9. Armulik, A. *et al.* Pericytes regulate the blood-brain barrier. *Nature* **468**, 557–561 (2010).
10. Daneman, R., Zhou, L., Kebede, A. A. & Barres, B. A. Pericytes are required for blood-brain barrier integrity during embryogenesis. *Nature* **468**, 562–566 (2010).
11. Vazquez-Liebanas, E. *et al.* Adult-induced genetic ablation distinguishes PDGFB roles in blood-brain barrier maintenance and development. *J. Cereb. Blood Flow Metab.* **42**, 264–279 (2022).
12. Gerhardt, H. & Betsholtz, C. Endothelial-pericyte interactions in angiogenesis. *Cell Tissue Res.* **314**, 15–23 (2003).

13. von Tell, D., Armulik, A. & Betsholtz, C. Pericytes and vascular stability. *Exp. Cell Res.* **312**, 623–629 (2006).
14. Lindblom, P. *et al.* Endothelial PDGF-B retention is required for proper investment of pericytes in the microvessel wall. *Genes Dev.* **17**, 1835–1840 (2003).
15. Watson, A. N. *et al.* Mild pericyte deficiency is associated with aberrant brain microvascular flow in aged PDGFRβ+/- mice. *J. Cereb. Blood Flow Metab. Off. J. Int. Soc. Cereb. Blood Flow Metab.* **40**, 2387–2400 (2020).
16. Bell, R. D. *et al.* Pericytes control key neurovascular functions and neuronal phenotype in the adult brain and during brain aging. *Neuron* **68**, 409–427 (2010).
17. Kisler, K. *et al.* Acute Ablation of Cortical Pericytes Leads to Rapid Neurovascular Uncoupling. *Front. Cell. Neurosci.* **14**, 27 (2020).
18. Cashion, J. M. *et al.* Pericyte ablation causes hypoactivity and reactive gliosis in adult mice. *Brain. Behav. Immun.* **123**, 681–696 (2025).
19. Choe, Y.-G. *et al.* Pericyte Loss Leads to Capillary Stalling Through Increased Leukocyte-Endothelial Cell Interaction in the Brain. *Front. Cell. Neurosci.* **16**, 848764 (2022).
20. Nikolakopoulou, A. M. *et al.* Pericyte loss leads to circulatory failure and pleiotrophin depletion causing neuron loss. *Nat. Neurosci.* **22**, 1089–1098 (2019).
21. Sengillo, J. D. *et al.* Deficiency in mural vascular cells coincides with blood-brain barrier disruption in Alzheimer's disease. *Brain Pathol. Zurich Switz.* **23**, 303–310 (2013).
22. Halliday, M. R. *et al.* Accelerated pericyte degeneration and blood-brain barrier breakdown in apolipoprotein E4 carriers with Alzheimer's disease. *J. Cereb. Blood Flow Metab.* **36**, 216–227 (2016).
23. Ding, R. *et al.* Loss of capillary pericytes and the blood-brain barrier in white matter in poststroke and vascular dementias and Alzheimer's disease. *Brain Pathol. Zurich Switz.* **30**, 1087–1101 (2020).

643 24. Davis, J. *et al.* Early-onset and robust cerebral microvascular accumulation of amyloid beta-
644 protein in transgenic mice expressing low levels of a vasculotropic Dutch/Iowa mutant form
645 of amyloid beta-protein precursor. *J. Biol. Chem.* **279**, 20296–20306 (2004).
646 25. Miao, J. *et al.* Cerebral microvascular amyloid beta protein deposition induces vascular
647 degeneration and neuroinflammation in transgenic mice expressing human vasculotropic
648 mutant amyloid beta precursor protein. *Am. J. Pathol.* **167**, 505–515 (2005).
649 26. Thal, D. R. *et al.* Two types of sporadic cerebral amyloid angiopathy. *J. Neuropathol. Exp.*
650 *Neurol.* **61**, 282–293 (2002).
651 27. Park, L. *et al.* Age-dependent neurovascular dysfunction and damage in a mouse model of
652 cerebral amyloid angiopathy. *Stroke* **45**, 1815–1821 (2014).
653 28. Nielson, C. D., Berthiaume, A.-A., Bonney, S. K. & Shih, A. Y. In vivo Single Cell Optical
654 Ablation of Brain Pericytes. *Front. Neurosci.* **16**, 900761 (2022).
655 29. Schager, B. & Brown, C. E. Susceptibility to capillary plugging can predict brain region
656 specific vessel loss with aging. *J. Cereb. Blood Flow Metab. Off. J. Int. Soc. Cereb. Blood*
657 *Flow Metab.* **40**, 2475–2490 (2020).
658 30. Reeson, P., Choi, K. & Brown, C. E. VEGF signaling regulates the fate of obstructed
659 capillaries in mouse cortex. *eLife* **7**, e33670 (2018).
660 31. Blinder, P. *et al.* The cortical angiome: an interconnected vascular network with
661 noncolumnar patterns of blood flow. *Nat. Neurosci.* **16**, 889–897 (2013).
662 32. Bonney, S. K., Nielson, C. D., Sosa, M. J., Bonnar, O. & Shih, A. Y. Capillary regression
663 leads to sustained local hypoperfusion by inducing constriction of upstream transitional
664 vessels. *Proc. Natl. Acad. Sci. U. S. A.* **121**, e2321021121 (2024).
665 33. Roy, T. K. & Secomb, T. W. Functional implications of microvascular heterogeneity for
666 oxygen uptake and utilization. *Physiol. Rep.* **10**, e15303 (2022).
667 34. Vestergaard, M. B. *et al.* Capillary transit time heterogeneity inhibits cerebral oxygen
668 metabolism in patients with reduced cerebrovascular reserve capacity from steno-occlusive

disease. *J. Cereb. Blood Flow Metab. Off. J. Int. Soc. Cereb. Blood Flow Metab.* **43**, 460–475 (2023).

35. Li, B. *et al.* More homogeneous capillary flow and oxygenation in deeper cortical layers correlate with increased oxygen extraction. *eLife* **8**, e42299 (2019).
36. Li, Y., Wei, W. & Wang, R. K. Capillary flow homogenization during functional activation revealed by optical coherence tomography angiography based capillary velocimetry. *Sci. Rep.* **8**, 4107 (2018).
37. Gutiérrez-Jiménez, E. *et al.* Effect of electrical forepaw stimulation on capillary transit-time heterogeneity (CTH). *J. Cereb. Blood Flow Metab. Off. J. Int. Soc. Cereb. Blood Flow Metab.* **36**, 2072–2086 (2016).
38. Hartmann, D. A., Coelho-Santos, V. & Shih, A. Y. Pericyte Control of Blood Flow Across Microvascular Zones in the Central Nervous System. *Annu. Rev. Physiol.* **84**, 331–354 (2022).
39. Wang, X. *et al.* Decreased Retinal Vascular Density in Alzheimer's Disease (AD) and Mild Cognitive Impairment (MCI): An Optical Coherence Tomography Angiography (OCTA) Study. *Front. Aging Neurosci.* **12**, 572484 (2020).
40. Zhang, X. *et al.* High-resolution mapping of brain vasculature and its impairment in the hippocampus of Alzheimer's disease mice. *Natl. Sci. Rev.* **6**, 1223–1238 (2019).
41. Xu, X. *et al.* Dynamic changes in vascular size and density in transgenic mice with Alzheimer's disease. *Aging* **12**, 17224–17234 (2020).
42. Buscho, S. *et al.* Longitudinal characterization of retinal vasculature alterations with optical coherence tomography angiography in a mouse model of tauopathy. *Exp. Eye Res.* **224**, 109240 (2022).
43. Bienvenu, K. & Granger, D. N. Molecular determinants of shear rate-dependent leukocyte adhesion in postcapillary venules. *Am. J. Physiol.* **264**, H1504-1508 (1993).

694 44. Singh, V., Kaur, R., Kumari, P., Pasricha, C. & Singh, R. ICAM-1 and VCAM-1: Gatekeepers
695 in various inflammatory and cardiovascular disorders. *Clin. Chim. Acta* **548**, 117487 (2023).
696 45. Salian, V. S. *et al.* Molecular Mechanisms Underlying Amyloid Beta Peptide Mediated
697 Upregulation of Vascular Cell Adhesion Molecule-1 in Alzheimer Disease. *J. Pharmacol.*
698 *Exp. Ther.* **391**, 430–440 (2024).
699 46. Yousef, H. *et al.* Aged blood impairs hippocampal neural precursor activity and activates
700 microglia via brain endothelial cell VCAM1. *Nat. Med.* **25**, 988–1000 (2019).
701 47. Zuliani, G. *et al.* Markers of endothelial dysfunction in older subjects with late onset
702 Alzheimer's disease or vascular dementia. *J. Neurol. Sci.* **272**, 164–170 (2008).
703 48. Frohman, E. M., Frohman, T. C., Gupta, S., de Fougerolles, A. & van den Noort, S.
704 Expression of intercellular adhesion molecule 1 (ICAM-1) in Alzheimer's disease. *J. Neurol.*
705 *Sci.* **106**, 105–111 (1991).
706 49. Manda-Handzlik, A. & Demkow, U. The Brain Entangled: The Contribution of Neutrophil
707 Extracellular Traps to the Diseases of the Central Nervous System. *Cells* **8**, 1477 (2019).
708 50. Bach, F. H., Hancock, W. W. & Ferran, C. Protective genes expressed in endothelial cells: a
709 regulatory response to injury. *Immunol. Today* **18**, 483–486 (1997).
710 51. Iliff, J. J. *et al.* A paravascular pathway facilitates CSF flow through the brain parenchyma
711 and the clearance of interstitial solutes, including amyloid β. *Sci. Transl. Med.* **4**, 147ra111
712 (2012).
713 52. Peng, W. *et al.* Suppression of glymphatic fluid transport in a mouse model of Alzheimer's
714 disease. *Neurobiol. Dis.* **93**, 215–225 (2016).
715 53. Bracko, O., Cruz Hernández, J. C., Park, L., Nishimura, N. & Schaffer, C. B. Causes and
716 consequences of baseline cerebral blood flow reductions in Alzheimer's disease. *J. Cereb.*
717 *Blood Flow Metab.* **41**, 1501–1516 (2021).
718 54. Madsen, L. S. *et al.* Capillary function progressively deteriorates in prodromal Alzheimer's
719 disease: A longitudinal MRI perfusion study. *Aging Brain* **2**, 100035 (2022).

55. Nielsen, R. B. *et al.* Impaired perfusion and capillary dysfunction in prodromal Alzheimer's disease. *Alzheimers Dement. Amst. Neth.* **12**, e12032 (2020).
56. Custodia, A. *et al.* Biomarkers Assessing Endothelial Dysfunction in Alzheimer's Disease. *Cells* **12**, 962 (2023).
57. Kalaria, R. N. & Hedera, P. Differential degeneration of the cerebral microvasculature in Alzheimer's disease. *Neuroreport* **6**, 477–480 (1995).
58. Lai, A. Y. *et al.* Venular degeneration leads to vascular dysfunction in a transgenic model of Alzheimer's disease. *Brain J. Neurol.* **138**, 1046–1058 (2015).
59. Stamenkovic, S. *et al.* Impaired capillary-venous drainage contributes to gliosis and demyelination in mouse white matter during aging. *Nat. Neurosci.* https://doi.org/10.1038/s41593-025-02023-z (2025) doi:10.1038/s41593-025-02023-z.
60. McDowell, K. P., Berthiaume, A.-A., Tieu, T., Hartmann, D. A. & Shih, A. Y. VasoMetrics: unbiased spatiotemporal analysis of microvascular diameter in multi-photon imaging applications. *Quant. Imaging Med. Surg.* **11**, 969–982 (2021).

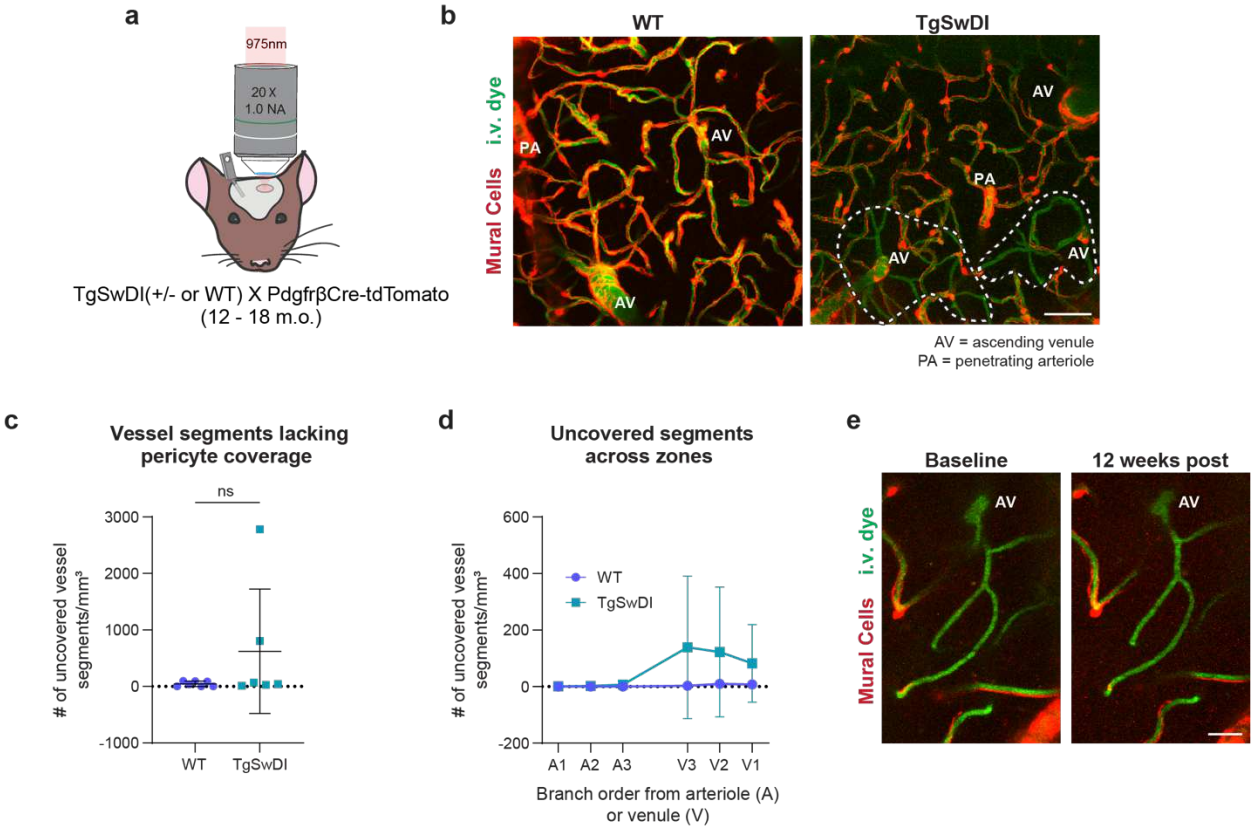

Figure 1. Uncovered capillaries in Tg-SwDI mice are found closer to the venule side of the microvascular network. a) Schematic of in vivo two-photon imaging and breeding scheme for experiments. **b)** Representative *in vivo* two-photon image of cortex from a wild-type (WT) mouse and a Tg-SwDI mouse with pericyte loss in peri-venous capillaries. Vessels shown in green and mural cells shown in red. Regions lacking pericyte coverage indicated with white dotted lines. AV=ascending venule. PA=penetrating arteriole. Scale bar=50μm. **c)** Graph showing the total number of vessel segments lacking pericyte coverage in WT and Tg-SwDI mice. Two-tailed Mann-Whitney test: p=0.3619. WT n=7 mice, Tg-SwDI n=6 mice. Data shown as mean ± SD. **d)** Graph showing the number of vessel segments lacking pericyte coverage in WT and Tg-SwDI mice sorted by branch order from penetrating arteriole (A) or ascending venule (V). Two-way ANOVA with Sidak's multiple comparisons: Effect of genotype: $F(1,66)=5.823$, *p=0.0186, Effect of location: $F(5,66)=1.403$, p=0.2348, interaction: $F(5,66)=1.141$, p=0.3478. WT n=7 mice, Tg-SwDI n=6 mice. Data shown as mean ± SD. **e)** Representative images of uncovered vessels in a Tg-SwDI mouse 12 weeks apart. Vessels shown in green and mural cells shown in red. AV=ascending venule. Scale bar=20μm.

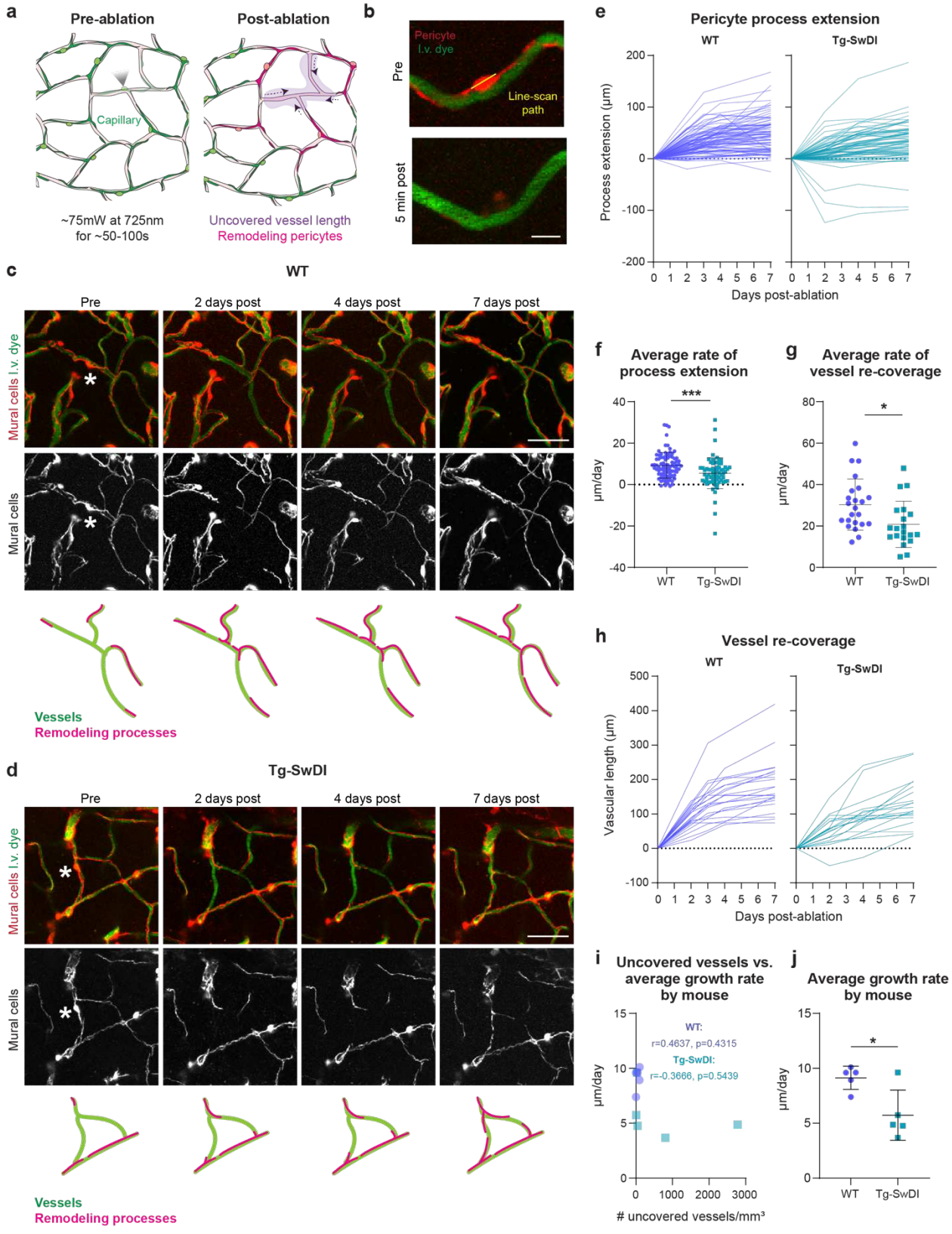
a
Pre-ablation
Post-ablation
Capillary
~75mW at 725nm
for ~50-100s
Uncovered vessel length
Remodeling pericytes
b
Pericyte
I.v. dye
Line-scan
path
Pre
5 min post
c
WT
Pre
2 days post
4 days post
7 days post
Mural cells I.v. dye
Mural cells
Vessels
Remodeling processes
d
Tg-SwDI
Pre
2 days post
4 days post
7 days post
Mural cells I.v. dye
Mural cells
Vessels
Remodeling processes
e
Pericyte process extension
WT
Tg-SwDI
Process extension (µm)
Days post-ablation
f
Average rate of
process extension
***
µm/day
WT
Tg-SwDI
g
Average rate of
vessel re-coverage
*
µm/day
WT
Tg-SwDI
h
Vessel re-coverage
WT
Tg-SwDI
Vascular length (µm)
Days post-ablation
i
Uncovered vessels vs.
average growth rate
by mouse
WT:
r=0.4637, p=0.4315
Tg-SwDI:
r=-0.3666, p=0.5439
µm/day
uncovered vessels/mm³
j
Average growth rate
by mouse
*
µm/day
WT
Tg-SwDI

Figure 2. Pericyte remodeling rate is decreased in Tg-SwDI mice. a) Schematic of a pericyte ablation showing target pericyte (left), uncovered vasculature following ablation (right, purple), and remodeling pericytes (right, pink). Black arrows=direction of process growth. **b)** Example *in vivo* images of a pericyte (red) and vessel (green) before and 5 minutes post-ablation. Yellow line=ablative line-scan path. Scale bar=10μm. **c,d)** Representative examples of pericyte remodeling in a WT (c) and Tg-SwDI (d) mouse. In top panels, pericytes shown in red and vessels shown in green. In the bottom panels, only mural cells are shown. White asterisk=target pericyte. Schematics of pericyte remodeling over time depicted under images with vessels in green and pericyte processes in pink. Scale bar=50μm. **e)** Graphs of individual pericyte process extension over time in WT (left) and Tg-SwDI (right) mice. **f)** Graph of average pericyte process growth rate in each genotype. Two-tailed Mann-Whitney test: ***p=0.002. Data shown as mean ± SD. n=5 mice/group (86 processes from 23 WT ablations and 69 processes from 20 Tg-SwDI ablations). **g)** Graph of the average rate of vessel re-coverage in each genotype. Two-tailed, nested t-test: $F(1,41)=7.011$, *p=0.0114. Data shown as mean ± SD. n=5 mice/group (23 WT ablations and 20 Tg-SwDI ablations). **h)** Graph of vascular re-coverage over time after pericyte ablation in WT (left) and Tg-SwDI (right) mice. **i)** Correlation plot of the number of vessel segments lacking pericyte coverage vs. the average growth rate of pericyte processes per mouse in each genotype. Two-tailed Pearson correlation tests. R and p values reported on graph. n=5 mice/group. **j)** Graph of average pericyte process growth rate per mouse in each genotype. Two-tailed, unpaired t-test: $F(4,4)=4.698$, *p=0.0167. n=5 mice/group.

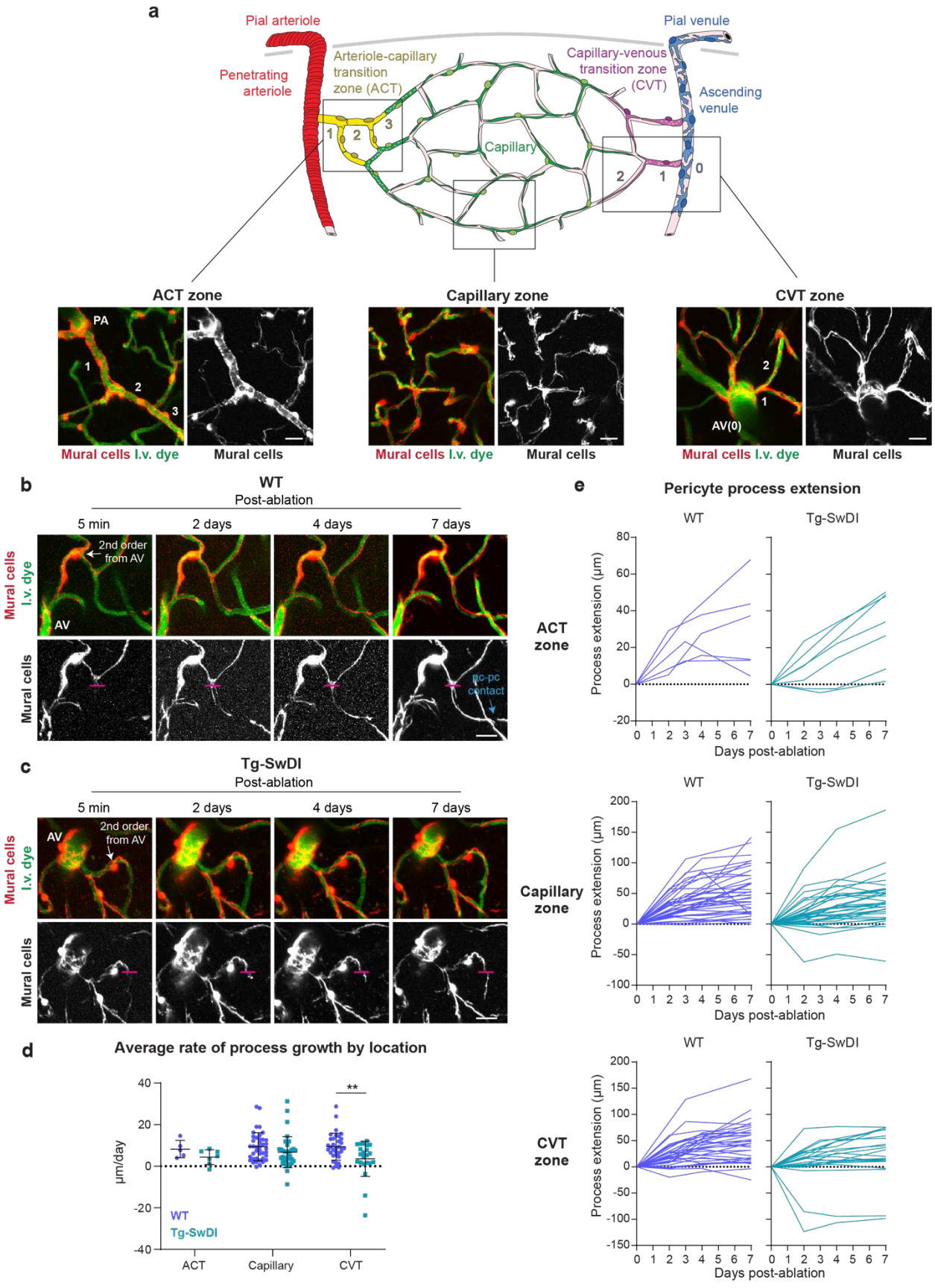
a
Pial arteriole
Penetrating arteriole
Arteriole-capillary transition zone (ACT)
Capillary-venous transition zone (CVT)
Pial venule
Ascending venule
Capillary
ACT zone
Capillary zone
CVT zone
PA
AV(0)
Mural cells l.v. dye
Mural cells
b
WT
Post-ablation
5 min
2 days
4 days
7 days
2nd order from AV
AV
pc-pc contact
c
Tg-SwDI
d
Average rate of process growth by location
μm/day
WT
Tg-SwDI
ACT
Capillary
CVT
**
e
Pericyte process extension
Process extension (μm)
Days post-ablation
ACT zone
Capillary zone
CVT zone

Figure 3. The capillary-venous transition zone exhibits the largest pericyte remodeling deficit in Tg-SwDI mice. a) Schematic of each zone of the cortical microvascular network. The ACT zone was classified as branch orders 1-3 from a penetrating arteriole (PA), the CVT zone was classified as the ascending venule (AV) and branch orders 1-2 from an AV, and the capillary zone was classified as vessels >3 branch orders from a PA and >2 branch orders from an AV. In left panels, vessels shown in green and mural cells shown in red. Right panels show only mural cell channel. Scale bar=20μm. **b,c)** Representative examples of a remodeling pericyte in the CVT zone in a (b) WT and (c) Tg-SwDI mouse. In top panels, pericytes shown in red and vessels shown in green. Bottom panels show mural cell channel only. Arrowhead indicates the soma of the remodeling pericyte. Magenta bar indicates baseline process length to demonstrate growth of process over time. Pericyte-pericyte contact (pc-pc contact) is indicated with a blue arrowhead. AV=ascending venule. Scale bar=20μm. **d)** Graph of the average pericyte process growth rate of pericytes in each microvascular zone across WT and Tg-SwDI mice. Two-way ANOVA with Sidak's multiple comparisons: effect of genotype: $F(1,139)=6.571$, $^{*}p=0.0114$, effect of zone: $F(2,139)=0.9413$, $p=0.3926$, interaction: $F(2,139)=0.8459$, $p=0.4314$. ACT zone WT vs. Tg-SwDI: $p=0.7201$, capillary zone WT vs. Tg-SwDI: $p=0.2882$, CVT zone WT vs. Tg-SwDI: $^{**}p=0.0083$. n=5 mice/group (23 WT ablations and 20 Tg-SwDI ablations). Data shown as mean ± SD. **e)** Graph of individual pericyte process extension across the ACT zone (top), capillary zone (middle), and CVT zone (bottom).

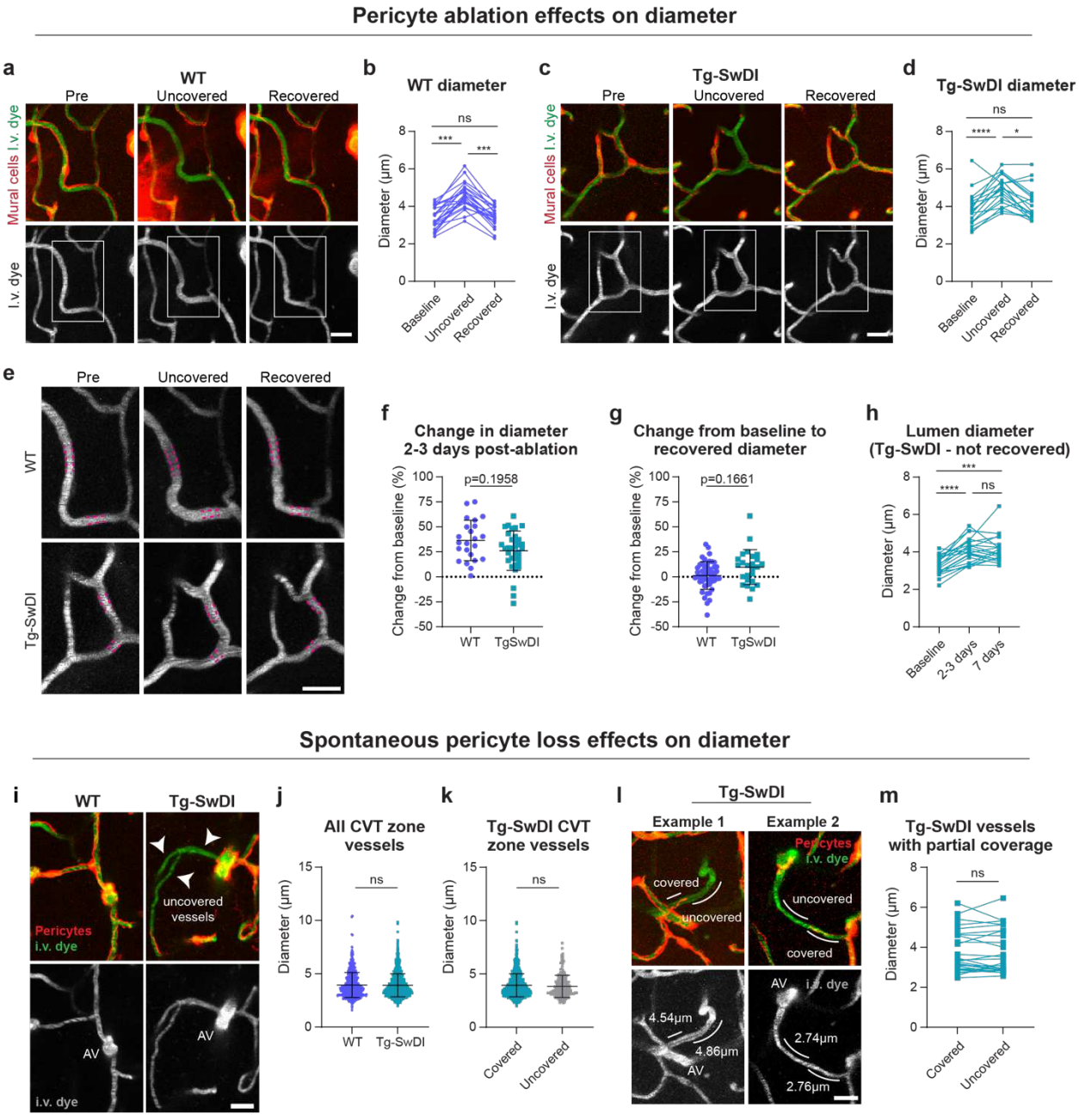

Figure 4. Pericyte ablations and spontaneous pericyte loss elicit different effects on capillary diameter. a) Images of WT vessels throughout pericyte remodeling. In top panels, vessels shown in green and pericytes shown in red. In lower panels, vessels shown in grey. Scale bar=20µm. **b**) Graph of WT capillary diameter throughout pericyte remodeling. Linear mixed effects model with Sidak's multiple comparisons: Effect of coverage: F(2,46.645)=32.015, ***p=<0.001, pre vs. uncovered: ***p<0.001, uncovered vs. recovered: ***p<0.001, pre vs. recovered: p=0.942. n=5 WT mice (23 capillaries). **c)** Images of Tg-SwDI vessels after pericyte ablation and remodeling. In top panels, vessels shown in green and pericytes shown in red. In bottom panels, vessels shown in grey. Scale bar=20µm**. d)** Graph of Tg-SwDI capillary diameter throughout pericyte remodeling. Friedman test with Dunn's multiple comparisons: Effect of

coverage: ****p<0.0001, pre vs. uncovered: ****p<0.0001, uncovered vs. recovered: *p=0.0449, pre vs. recovered: p=0.1547. n=5 Tg-SwDI mice (19 capillaries). **e)** Insets from (a) and (b). Dashed magenta lines=baseline diameter. Scale bar=20μm. **f)** Graph of percent change in capillary diameter post-ablation. Two-tailed Nested t-test: F(1,8)=1.992, p=0.1958. n=5 mice/group (23 WT and 34 Tg-SwDI capillaries). **g)** Graph of percent change from baseline to re-covered diameter. Two-tailed Nested t-test: F(1,8)=2.321, p=0.1661. n=5 mice/group (49 WT and 25 Tg-SwDI capillaries). **h)** Graph of capillary diameter in Tg-SwDI mice at baseline, 2-3 days after losing pericyte coverage, and 7 days after losing pericyte coverage. Friedman test with Dunn's multiple comparisons: Effect of coverage: ****p<0.0001, pre vs. 2-3 days: ****p<0.0001, 2-3 days vs. 7 days: p>0.9999, pre vs. 7 days: ***p=0.0002. n=5 Tg-SwDI mice (21 capillaries). **i)** Images of capillaries in WT and Tg-SwDI mice. In top panels, vessels shown in green and pericytes shown in red. In lower panels, vessels shown in grey. White arrowheads=uncovered vessels. AV=ascending venule. Scale bar=20μm. **j)** Capillary diameter of CVT zone vessels in WT and Tg-SwDI mice. Gamma mixed model: F(1,2551)=0.001, p=0.980. n=6 mice/group (864 WT and 1689 Tg-SwDI capillaries). **k)** Graph of capillary diameter of covered and uncovered CVT zone vessels in Tg-SwDI mice. Gamma mixed model: F(1,1687)=1.074, p=0.300. n=6 Tg-SwDI mice (1491 covered and 198 uncovered capillaries). **l)** Images of partially covered vessels in Tg-SwDI mice. In top panels, vessels shown in green and pericytes shown in red. In bottom panels, vessels shown in grey. White lines indicate where corresponding diameter measurements were taken. AV=ascending venule. Scale bar=20μm. **m)** Graph of partially covered vessel diameter. Wilcoxon matched-pairs signed rank test: p=0.8904. n=4 Tg-SwDI mice (26 capillaries). All error bars indicate mean ± SD.

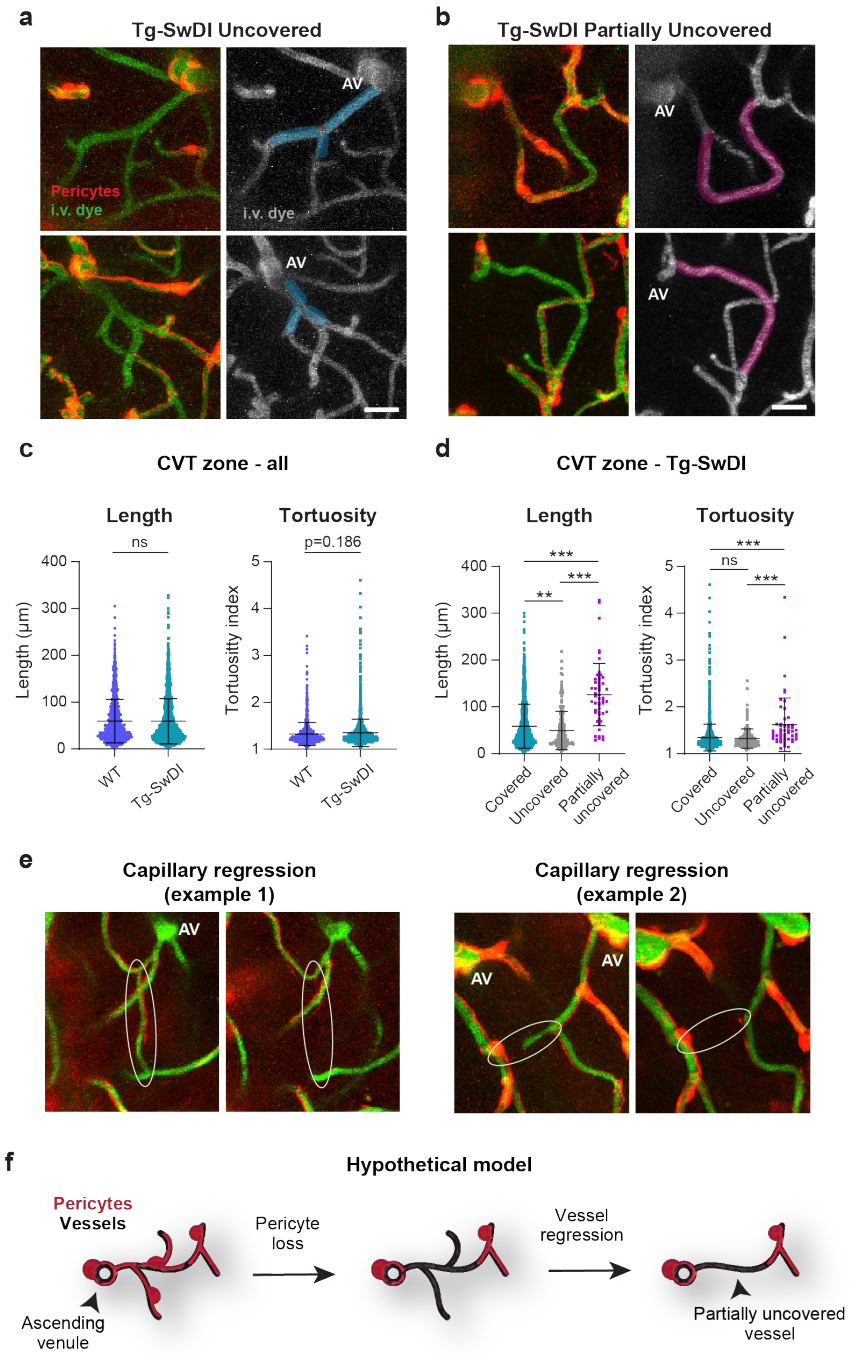

Figure 5. Spontaneous pericyte loss may lead to vessel regression. a) Images of fully uncovered vessels in Tg-SwDI mice. In the left panels, vessels shown in green and pericytes shown in red. In the right panels, vessels shown in grey. Examples of uncovered vessels traced in blue. AV=ascending venule. Scale bar=20µm. **b)** Images of partially uncovered vessels in Tg-SwDI mice. In the left panels, vessels shown in green and pericytes shown in red. In the right panels, vessels shown in grey. Examples of partially uncovered vessels traced in pink. AV=ascending venule. Scale bar=20µm. **c)** Graph of length (left) and tortuosity (right) of all CVT

zone vessels in WT and Tg-SwDI mice. Gamma mixed model for length: $F(1,3323)=0.003$, $p=0.954$. Gamma mixed model for tortuosity: $F(1,3323)=1.749$, $p=0.186$. n=7 WT and 6 Tg-SwDI mice (1133 WT capillaries, 2192 Tg-SwDI capillaries). Data shown as mean ± SD. **d)** Graph of length (left) and tortuosity (right) of covered, uncovered, and partially covered CVT zone vessels in Tg-SwDI mice. Gamma mixed models with Sidak's pairwise comparisons: Effect of pericyte coverage on length: $F(2,2189)=27.426$, ***p=<0.001, covered vs. uncovered: **p=0.006, covered vs. partially covered: ***p<0.001, uncovered vs. partially covered: ***p<0.001. Effect of pericyte coverage on tortuosity: $F(2,2189)=19.731$, ***p=<0.001, covered vs. uncovered: p=0.421, covered vs. partially covered: ***p<0.001, uncovered vs. partially covered: ***p<0.001. n=6 Tg-SwDI mice (1975 covered, 165 uncovered, 52 partially uncovered). Data shown as mean ± SD. **e)** Two examples of uncovered vessels in Tg-SwDI mice regressing after 12 weeks. Vessels shown in green and pericytes shown in red. AV=ascending venule. Scale bar=20μm. **f)** Schematic of a hypothetical model of vessel regression following pericyte loss. Pericytes shown in red and vessels shown in black.

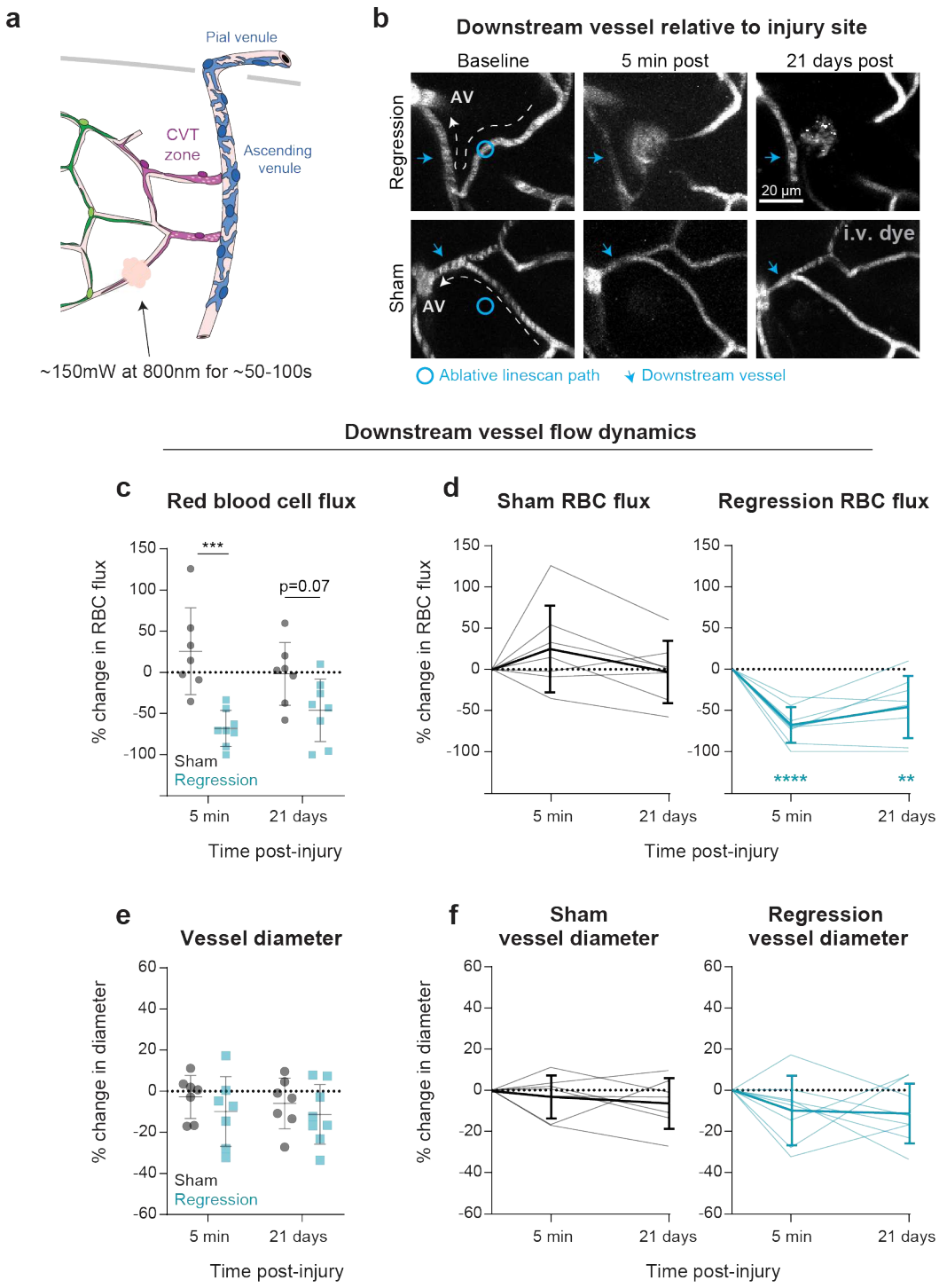

Figure 6. Capillary regression in CVT zone reduces blood flow into downstream drainage vessel. a) Schematic of optically-induced capillary injury in the CVT zone. **b)** Example of a capillary regression (top) and a sham (bottom) prior to, 5 min post, and 21 days post-injury. Blue circles = line-scan path, blue arrows = downstream vessel, white arrows = blood flow direction, AV=ascending venule. Vessels shown in grey. **c)** Graph of the percent change from baseline in

downstream vessel RBC flux 5 min and 21 days post-injury. Two-way repeated measures ANOVA with Sidak's multiple comparisons: Effect of injury type: $F(1,13)=13.81$, $^{**}p=0.0026$, effect of time: $F(1,13)=0.1296$, $p=0.7247$, interaction: $F(1,13)=11.01$, $^{**}p=0.0056$. Sham vs. regression 5 min post-injury: $^{***}p=0.0002$, sham vs. regression 21 days post-injury: $p=0.0709$. **d)** Graphs of the percent change from baseline in downstream vessel RBC flux 5 min and 21 days post-injury in sham (left) and regression (right) experiments. Two-way repeated measures ANOVA with Sidak's multiple comparisons: Effect of injury type: $F(1,13)=13.81$, $^{**}p=0.0026$, effect of time: $F(2,26)=4.024$, $^{*}p=0.0300$, interaction: $F(2,26)=12.90$, $^{***}p=0.0001$. Regression experiments: Pre vs. 5 min post-injury: $^{****}p<0.0001$, pre vs. 21 days post-injury: $^{**}p=0.0023$. Sham experiments: Pre vs. 5 min post-injury: $p=0.1320$, pre vs. 21 days post-injury: $p=0.9889$. **e)** Graph of the percent change from baseline in downstream vessel diameter 5 min and 21 days post-injury. Linear mixed-effects model: Effect of injury type: $F(1,13)=1.440$, $p=0.2515$, effect of time: $F(1,12)=0.1980$, $p=0.6643$, interaction: $F(1,12)=0.03028$, $p=0.8648$. **f)** Graphs of the percent change from baseline in downstream vessel diameter 5 min and 21 days post-injury in sham (left) and regression (right) experiments. Linear mixed-effects model: Effect of injury type: $F(1,13)=1.969$, $p=0.1839$, effect of time: $F(2,25)=1.551$, $p=0.2317$, interaction: $F(2,25)=0.7916$, $p=0.4642$. All data shown as mean ± SD. n=3 mice, 4-6 injuries/mouse.

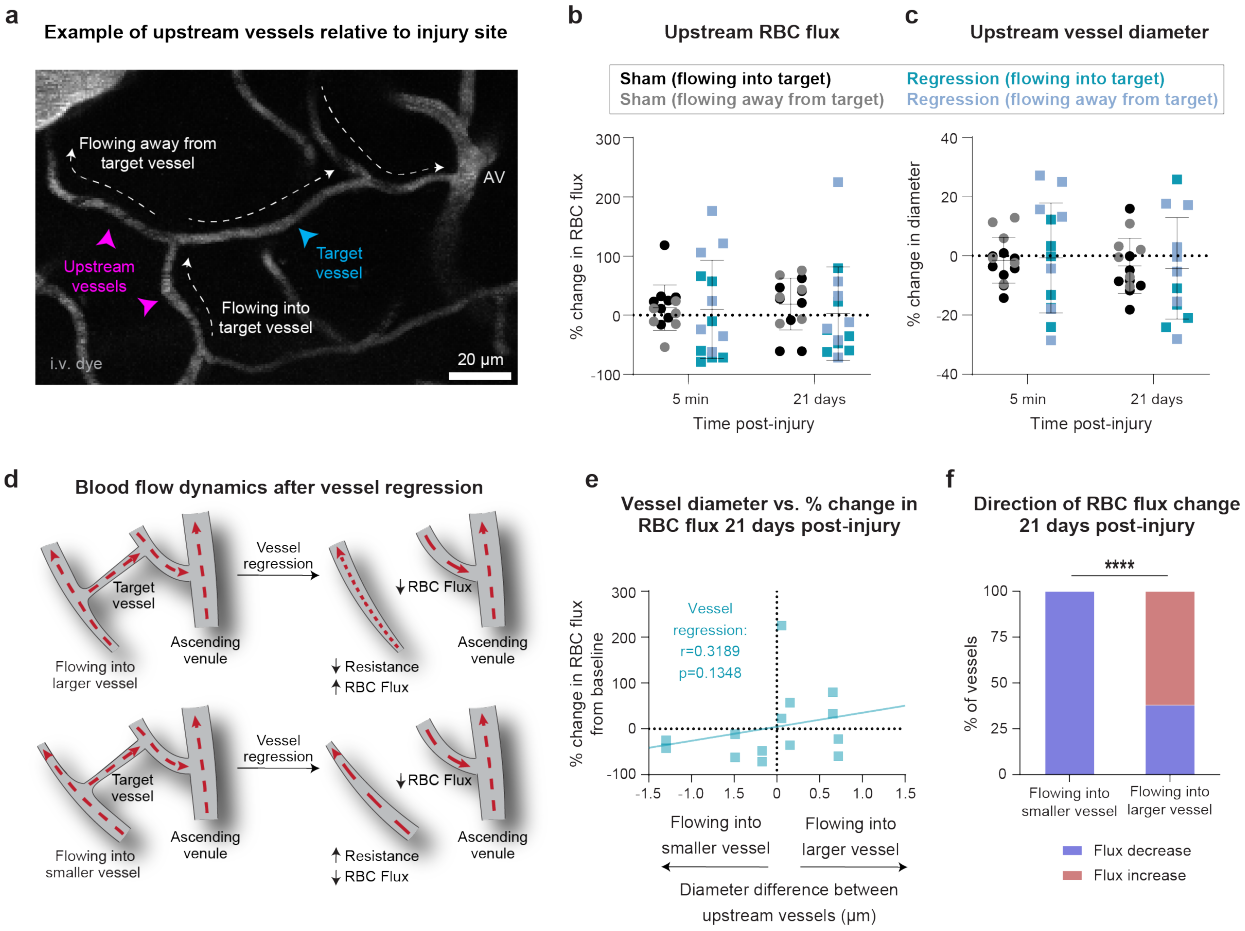

Figure 7. Capillary regression in CVT zone alters flow in upstream capillaries. a) Representative example of a capillary network targeted for regression experiments. The blue arrowhead depicts the target vessel. The magenta arrowheads depict the upstream vessels. The direction of blood flow is shown with white arrows. AV = ascending venule. Vessels shown in grey. Scale bar=20µm. **b)** Graph of percent change in RBC flux in upstream vessels at 5 min and 21 days-post injury. Two-way repeated-measures ANOVA: Effect of injury type: $F(1,26)=0.3793$, $p=0.5433$, effect of time: $F(1,26)=0.0007258$, $p=0.9787$, interaction: $F(1,26)=0.1251$, $p=0.7264$. Welch's F-test: 5 min post: $F(13,13)=4.704$, $^{**}p=0.0088$ and 21 days post: $F(13,13)=3.265$, $^{*}p=0.0416$. Data shown as mean ± SD. N=3 female mice, 2-3 capillary injuries and shams per mouse. **c)** Graph of percent change in vessel diameter in upstream vessels at 5 min and 21 days-post injury. Linear mixed model: Effect of injury type: $F(1,48.182)=0.226$, $p=0.637$, effect of time: $F(1,47.989)=0.684$, $p=0.412$, interaction: $F(1,47.989)=0.063$, $p=0.802$. Welch's F-test: 5 min post: $F(11,13)=6.314$, $^{**}p=0.0026$, and 21 days post: $F(11,13)=3.662$, $^{*}p=0.0295$. Data shown as mean ± SD. N=3 female mice, 2-3 capillary injuries and shams per mouse. **d)** Schematic of blood flow changes after capillary regression. Blood flow in the vessel downstream of the target vessel is consistently reduced. Upstream, if blood is flowing into a smaller diameter vessel, resistance increases and RBC flux decreases. Conversely, if blood is flowing into a larger diameter vessel, resistance decreases and RBC flux increases. **e)** Graph of diameter difference of upstream vessels vs. percent change in RBC flux from baseline at 21 days post-injury. One-tailed Spearman

correlation. R and p values reported on graph. n=14 pooled vessels from 7 regression experiments across 3 mice. **f)** Graph of the proportion of upstream vessels that decrease (blue) or increase (red) in flux compared between cases of flow into larger vessels versus flow into smaller vessels. One-sided Fisher's exact test: ****$p<0.0001$. n=14 pooled vessels from 7 regression experiments across 3 mice.

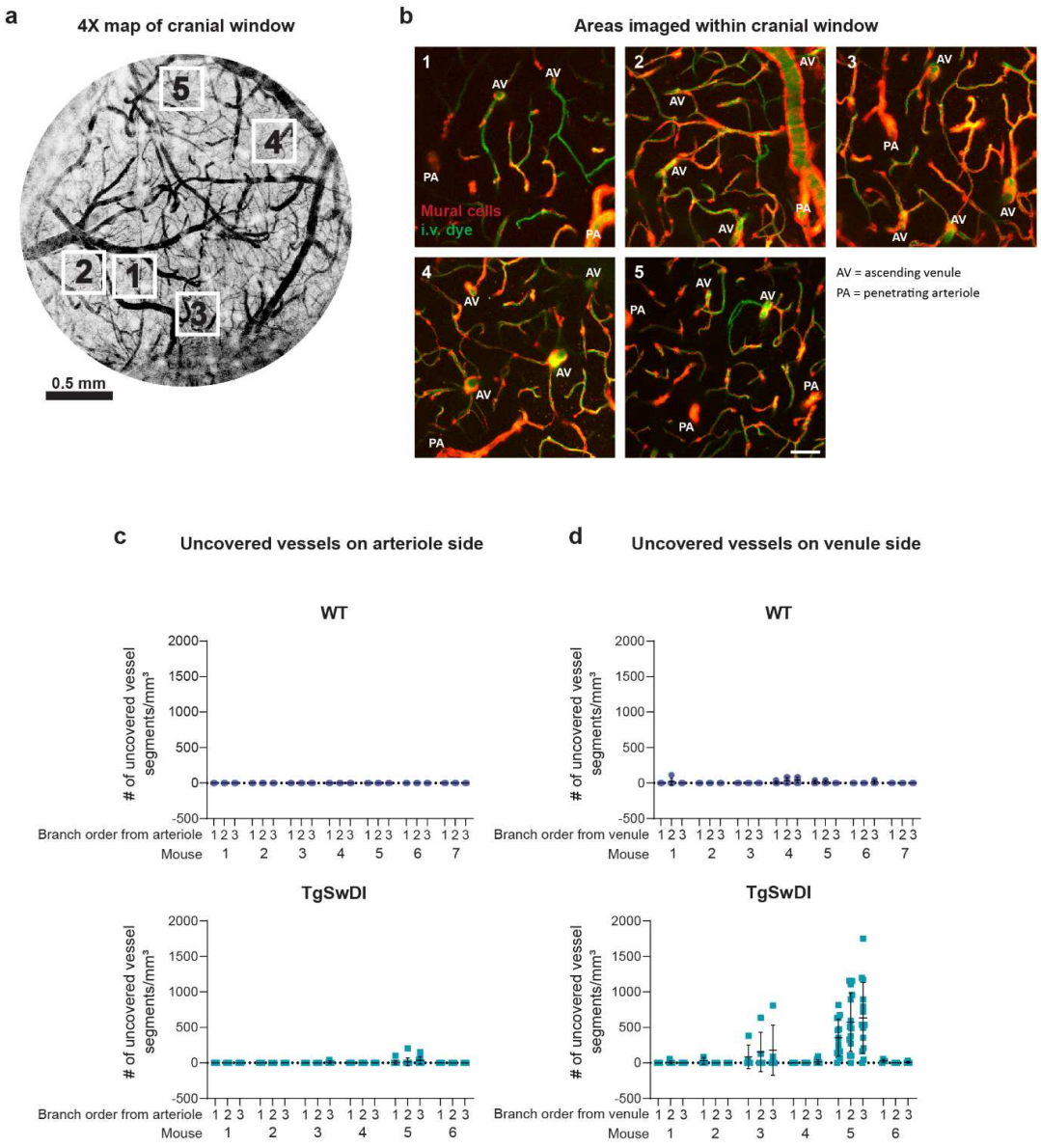

Supplemental Figure 1. Loss of pericyte coverage in Tg-SwDI mice is variable between and within mice. a) Example of an entire cranial window in a 17-month-old mouse. Vessels are shown in grey. White rectangles indicate regions imaged a high-resolution with a 20-X objective. Scale bar=0.5mm. **b)** Corresponding high-resolution images of regions marked in **a**. Mural cells are shown in red and vessels are shown in green. AV=ascending venule. PA=penetrating arteriole. Scale bar=50μm. **c)** Graphs of the number of vessel segments/mm^3 lacking pericyte coverage on branch orders 1-3 from PAs in each z-stack separated across individual mice. WT mice shown in the upper panel and Tg-SwDI mice shown in the lower panel. **d)** Graphs of the number of vessel segments/mm^3 lacking pericyte coverage on branch orders 1-3 from AVs in each z-stack separated across individual mice. WT mice shown in the upper panel and Tg-SwDI mice shown in the lower panel. All data are shown as mean ± SD. WT n=7 mice, Tg-SwDI n=6 mice.

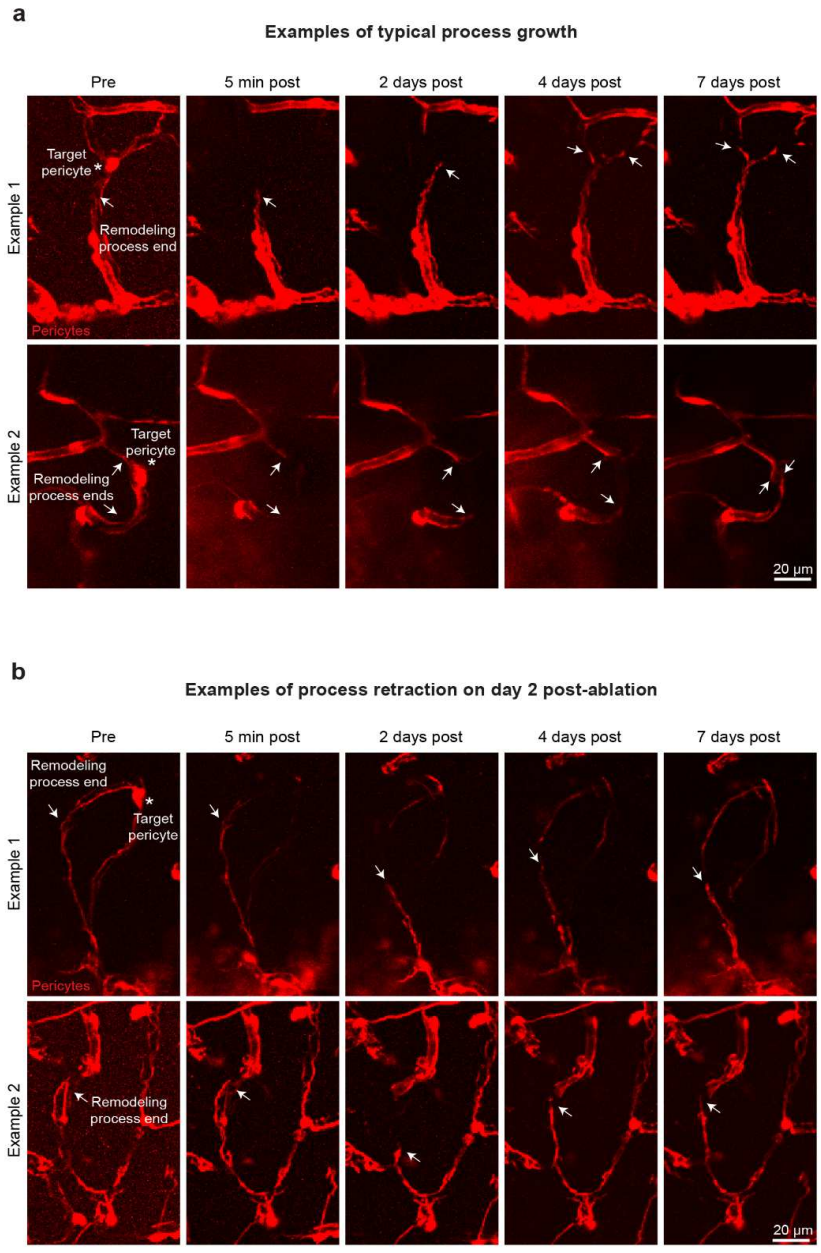

Supplemental Figure 2. Typical process growth compared to process retraction in Tg-SwDI mice. a) Two examples of pericyte process growth. Images are shown at baseline and 5 minutes, 2 days, 4 days, and 7 days post-ablation. Target pericyte indicated with a white asterisk. Remodeling process terminal tips indicated with white arrowheads. Pericytes are shown in red. Scale bar=20µm. **b)** Two examples of pericyte process retraction. Images are shown at baseline and 5 minutes, 2 days, 4 days, and 7 days post-ablation. Target pericyte indicated with a white asterisk. Remodeling process terminal tips indicated with white arrowheads. Target pericyte in Example 2 is not within the projected image. Pericytes are shown in red. Scale bar=20µm.

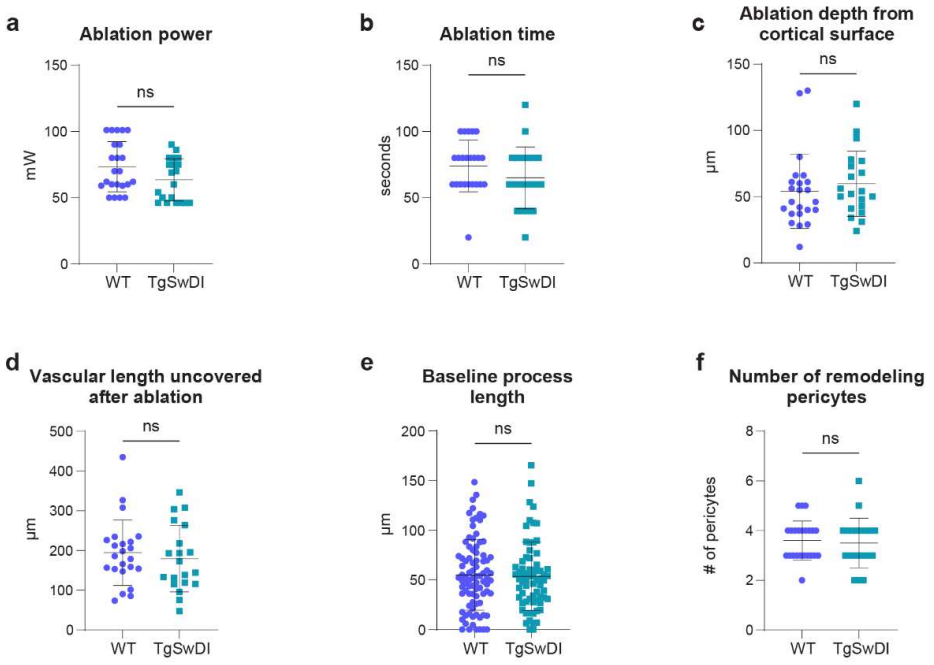

Supplemental Figure 3. Pericyte ablation parameters do not differ between WT and Tg-SwDI mice. a) Graph of laser power used to ablate each pericyte. Two-tailed Nested t-test: $F(1,8)=1.482$, $p=0.2581$. Data are shown as mean ± SD. n=5 mice/group, 3-6 ablations/mouse. **b)** Graph of laser irradiation time required to ablate each pericyte. Two-tailed Nested t-test: $F(1,8)=1.449$, $p=0.2631$. Data are shown as mean ± SD. n=5 mice/group, 3-6 ablations/mouse. **c)** Graph of target pericyte depth from cortical surface. Two-tailed Nested t-test: $F(1,8)=0.3836$, $p=0.5529$. Data are shown as mean ± SD. n=5 mice/group, 3-6 ablations/mouse. **d)** Graph of vascular length uncovered 5 minutes post-pericyte ablation. Two-tailed Nested t-test: $F(1,41)=0.3586$, $p=0.5526$. Data are shown as mean ± SD. n=5 mice/group, 3-6 ablations/mouse. **e)** Graph of baseline length of remodeling pericyte processes. Two-tailed Mann-Whitney test: $p=0.7508$. Data are shown as mean ± SD. n=5 mice/group, 9-25 processes/mouse. **f)** Graph of the number of remodeling pericytes in individual pericyte ablation experiments. Two-tailed Nested t-test: $F(1,41)=0.1596$, $p=0.6916$. Data are shown as mean ± SD. n=5 mice/group, 3-6 ablations/mouse.

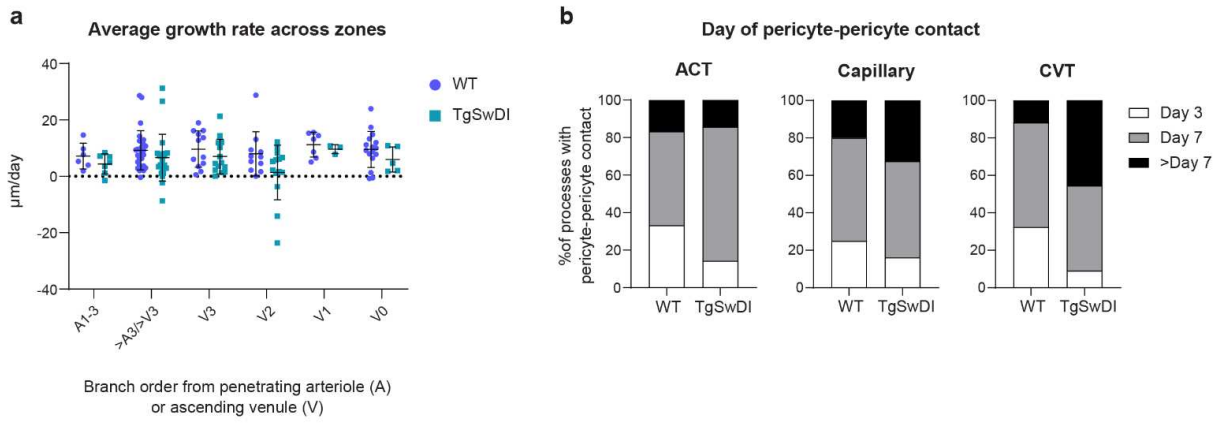

Supplemental Figure 4. Pericyte remodeling deficits across microvascular zones. a) Graph of average growth rate of pericyte processes based on cell body location from arteriole (A) or venule (V). Data are shown as mean ± SD. n=5 mice/group, 3-6 ablations/mouse, 9-25 processes/mouse. **b)** Graphs of the percent of total processes finished growing by timepoint in the ACT zone (left), capillary zone (middle), and CVT zone (right). Fisher's exact tests: ACT zone: **p=0.0029, capillary zone: p=0.0916, CVT zone: ****p<0.0001. Data pooled for analysis. n=5 mice/group, 3-6 ablations/mouse, 9-25 processes/mouse.

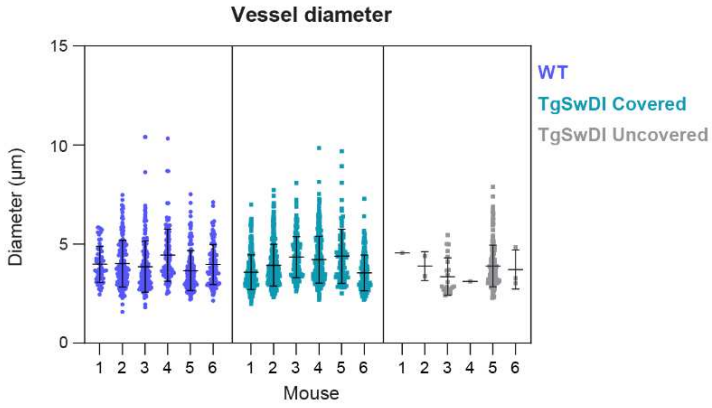

Supplemental Figure 5. Lumen diameters for CVT zone vessels. Graph of diameter measurements for all vessels in each mouse. n=6 mice/group.

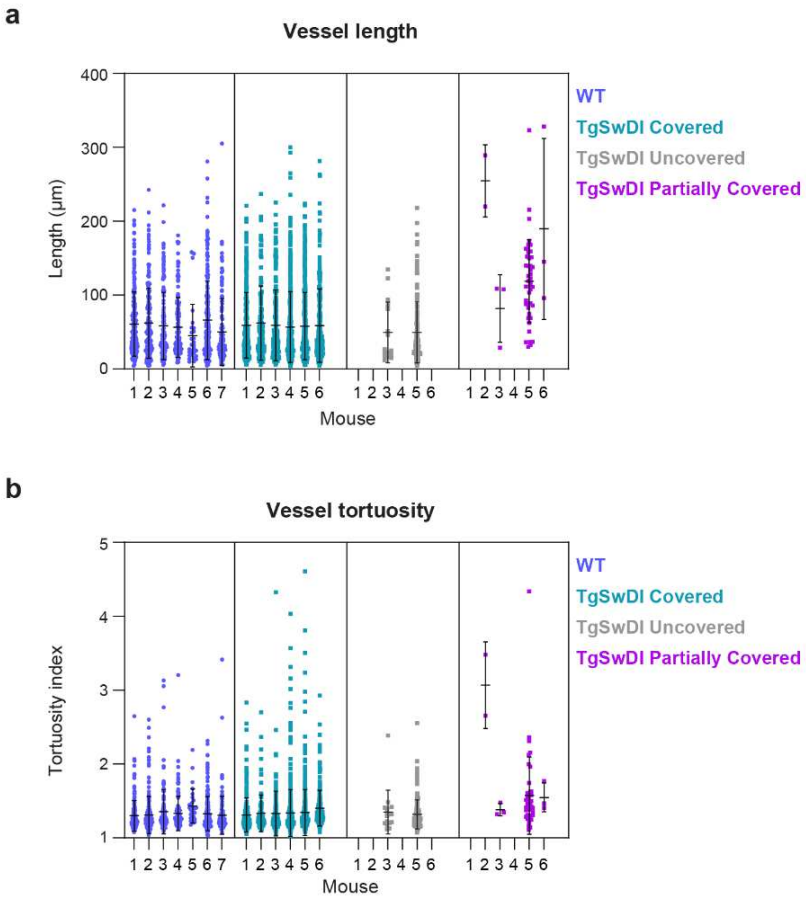

Supplemental Figure 6. Length and tortuosity measurements for CVT zone vessels. (a,b) Graph of **(a)** length and (**b)** tortuosity measurements for all vessels in each mouse. WT n=7 mice. Tg-SwDI n=6 mice.

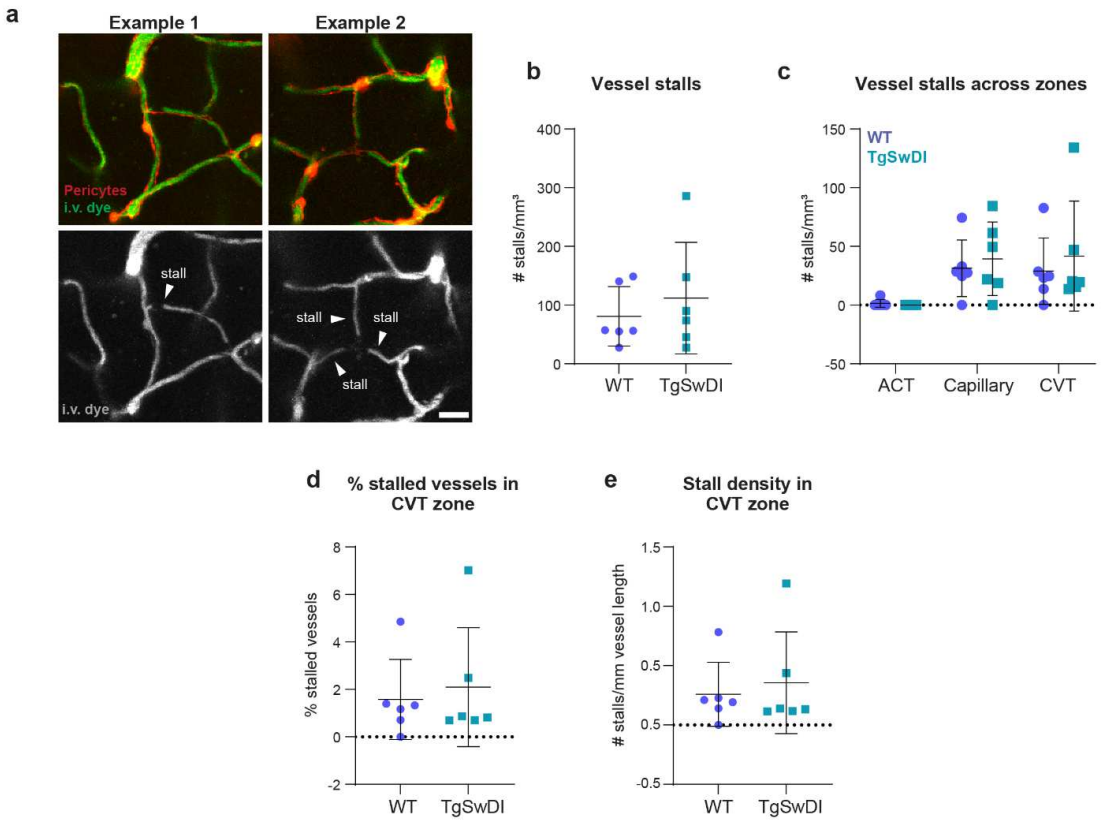

Supplemental Figure 7. Comparison of blood flow stalls detected in image stacks between Tg-SwDI mice and WT controls. a) Representative examples of blood flow stalling. In upper panels, vessels are shown in green and pericytes are shown in red. In lower panels, vessels are shown in grey. Stalls are indicated with white arrowheads. Scale bar=20μm. **b)** Graph of the number of stalls per cubic millimeter in WT and Tg-SwDI mice. Two-tailed Unpaired t-test: F(5,5)=3.507, p=0.4985. n=6 mice/group. **c)** Graph of the number of stalls per cubic millimeter across microvascular zones in WT and Tg-SwDI mice. Two-way ANOVA with Tukey's multiple comparisons. Effect of genotype: F(1,30)=0.4967, p=0.4864, effect of zone: F(2,30)=6.298, **p=0.0052, interaction: F(2,30)=0.2507, p=0.8153. ACT vs. Capillary: *p=0.0120, ACT vs. CVT: *p=0.0122, Capillary vs. CVT: p>0.9999. n=6 mice/group. **d)** Graph of the percent of stalled vessels in the CVT zone of WT and Tg-SwDI mice. Two-tailed Mann-Whitney test: p=0.9372. n=6 mice/group. **e)** Graph of the number of stalled vessels per mm of vessel length in the CVT zone of WT and Tg-SwDI mice. Two-tailed Mann-Whitney test: p=0.6991. All data are shown as mean ± SD. n=6 mice/group.

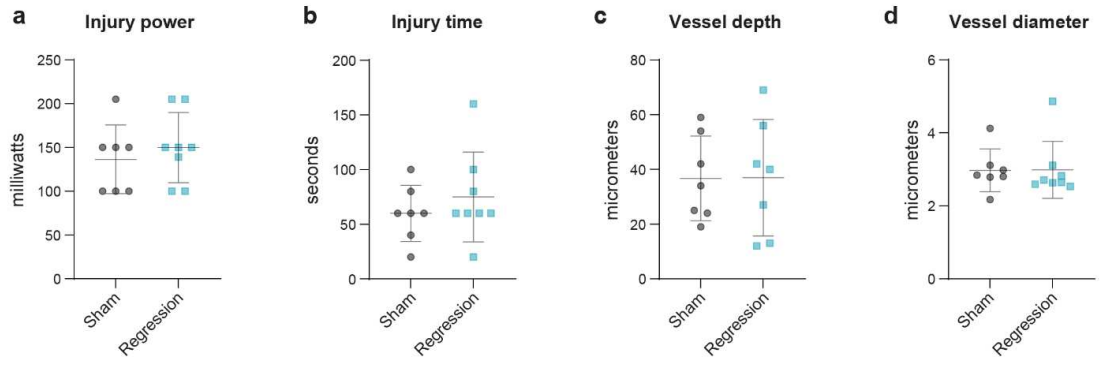

Supplemental Figure 8. Capillary injury parameters do not differ between sham and regression experiments. **a)** Graph of laser power used for injury experiments. Two-tailed Nested t-test: $F(1,4)=0.2738$, $p=0.6285$. **b)** Graph of laser irradiation time used for injury experiments. Two-tailed Nested t-test: $F(1,4)=0.4768$, $p=0.5279$. **c)** Graph of target vessel depth from cortical surface. Two-tailed Nested t-test: $F(1,13)=0.01349$, $p=0.9093$. **d)** Graph of target vessel diameter. Two-tailed Nested t-test: $F(1,4)=0.0003084$, $p=0.9868$. All data are shown as mean ± SD. n=3 mice, 4-6 injuries/mouse.

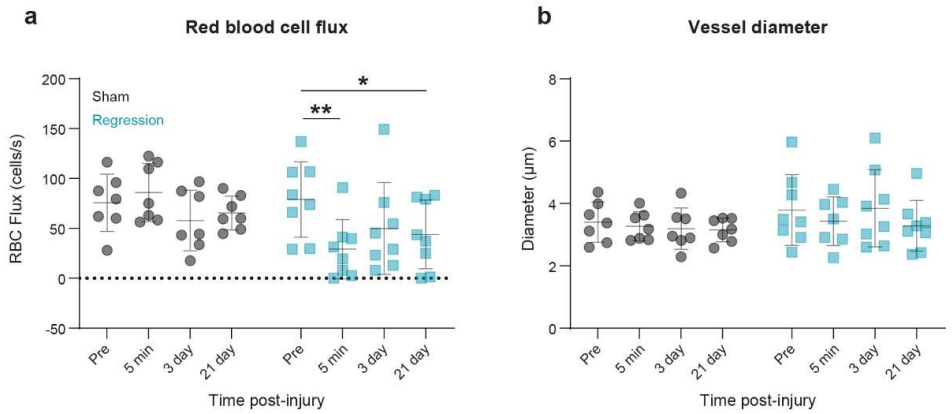

Supplemental Figure 9. Downstream vessel RBC flux and diameter 5 min, 3 days, and 21 days-post injury. a) Graph of downstream vessel red blood cell flux 5 min, 3 days, and 21 days post-injury in sham and regression experiments. Two-way repeated measures ANOVA with Sidak's multiple comparisons: Effect of injury type: $F(1,13)=2.212$, $p=0.1608$, effect of time: $F(2.033, 25.44)=3.791$, $^{*}p=0.0351$, interaction: $F(3,39)=5.226$, $^{**}p=0.0040$. For regression experiments: Pre vs. 5 min: $^{**}p=0.0015$, Pre vs. 3 days: $p=0.2423$, Pre vs. 21 days: $^{*}p=0.0390$. For sham experiments: Pre vs. 5 min: $p=0.7679$, Pre vs. 3 days: $p=0.6083$, Pre vs. 21 days: $p=0.7947$. **b)** Graph of downstream vessel diameter 5 min, 3 days, and 21 days post-injury in sham and regression experiments. Mixed-effects model: Effect of injury type: $F(1,44.979)=5.269$, $^{*}p=0.026$, effect of time: $F(3,21.833)=0.943$, $p=0.437$, interaction: $F(3,21.833)=0.396$, $p=0.757$. All data are shown as mean ± SD. n=3 mice, 2-3 shams/regressions per mouse.

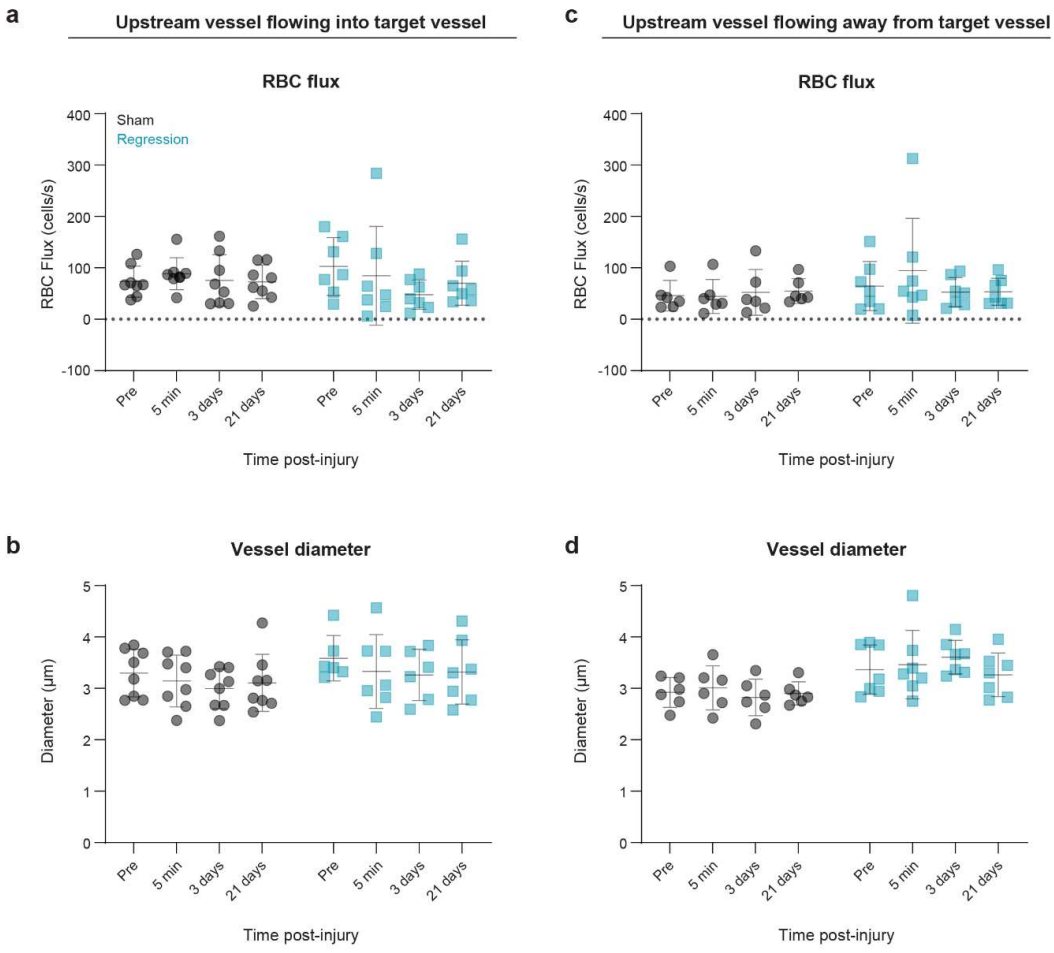

Supplemental Figure 10. Upstream vessel RBC flux and diameter 5 min, 3 days, and 21 days-post injury. a) Graph of upstream vessel (flowing into target vessel) red blood cell flux 5 min, 3 days, and 21 days post-injury in sham and regression experiments. Two-way repeated measures ANOVA: Effect of injury type: $F(1,13)=0.003906$, $p=0.9511$, effect of time: $F(1.937,25.18)=1.668$, $p=0.2093$, interaction: $F(3,39)=1.435$, $p=0.2473$. **b)** Graph of upstream vessel (flowing into target vessel) diameter flux 5 min, 3 days, and 21 days post-injury in sham and regression experiments. Mixed-effects model: Effect of injury type: $F(1,13)=1.050$, $p=0.3243$, effect of time: $F(1.845,22.75)=1.702$, $p=0.2059$, interaction: $F(3,37)=0.03307$, $p=0.9918$. **c)** Graph of upstream vessel (flowing away from target vessel) red blood cell flux 5 min, 3 days, and 21 days post-injury in sham and regression experiments. Two-way repeated measures ANOVA: Effect of injury type: $F(1,11)=0.7572$, $p=0.4028$, effect of time: $F(1.314,14.45)=0.4701$, $p=0.5553$, interaction: $F(3,33)=1.125$, $p=0.3531$. **d)** Graph of upstream vessel (flowing away from target vessel) diameter 5 min, 3 days, and 21 days post-injury in sham and regression experiments. Mixed-effects model: Effect of injury type: $F(1,11)=8.215$, $^*p=0.0153$, effect of time: $F(1.576,17.34)=0.6022$, $p=0.5208$, interaction: $F(3,33)=1.056$, $p=0.3810$. All data are shown as mean ± SD. n=3 mice, 2-3 shams/regressions per mouse.

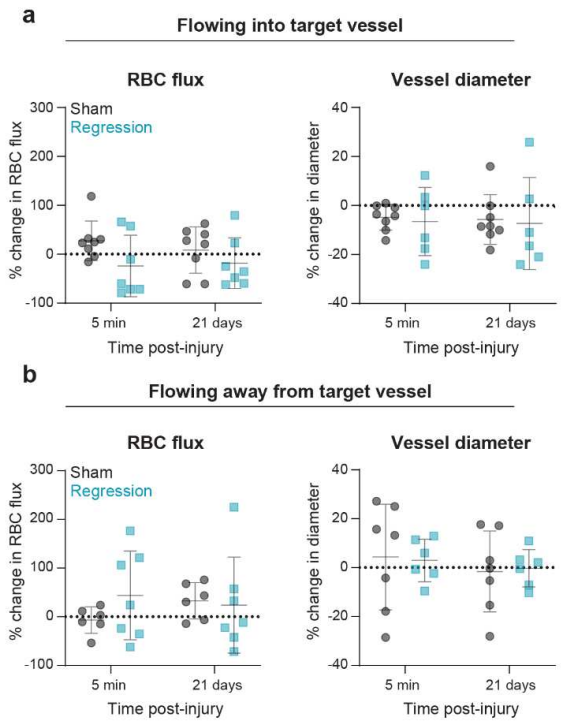

Supplemental Figure 11. Change in upstream vessel RBC flux and diameter. a) Graphs of percent change in RBC flux (left) and vessel diameter (right) in upstream vessels flowing into the target vessel at 5 min, 3 days, and 21 days-post injury. For RBC flux: Two-way repeated measures ANOVA: Effect of injury type: $F(1,13)=4.663$, $p=0.0501$, effect of time: $F(1,13)=0.1188$, $p=0.7359$, interaction: $F(1,13)=0.4203$, $p=0.5281$. For vessel diameter: Linear mixed-effects model: Effect of injury type: $F(1,18.982)=0.343$, $p=0.565$, effect of time: $F(1,18.546)=0.939$, $p=0.345$, interaction: $F(1,18.546)=0.084$, $p=0.775$. Data are shown as mean ± SD. n=3 female mice, 4-6 injuries/mouse. **b)** Graphs of percent change in RBC flux (left) and vessel diameter (right) in upstream vessels flowing away from the target vessel at 5 min, 3 days, and 21 days-post injury. For RBC flux: Two-way repeated measures ANOVA: Effect of injury type: $F(1,11)=0.9198$, $p=0.3581$, effect of time: $F(1,11)=0.07858$, $p=0.7844$, interaction: $F(1,11)=0.7363$, $p=0.4092$. For vessel diameter: Linear mixed-effects model: Effect of injury type: $F(1,18.409)=0.245$, $p=0.626$, effect of time: $F(1,18.321)=0.035$, $p=0.854$, interaction: $F(1,18.321)=0$, $p=0.988$. n=3 mice, 2-3 shams/regressions per mouse.